


HI absorption towards radio Active Galactic Nuclei of different accretion modes

Yogesh Chandola^{1,2,3} *, D.J. Saikia² and Di Li^{3,4,5}

¹Purple Mountain Observatory, Chinese Academy of Sciences, 10, Yuan Hua Road, Qixia District, Nanjing, 210023, China

²Inter-University Centre for Astronomy and Astrophysics (IUCAA), Post Bag 4, Ganeshkhind, Pune, 411007, India

³National Astronomical Observatories, Chinese Academy of Sciences, 20A, Datun Road, Chaoyang District, Beijing, 100101, China

⁴NAOC-UKZN Computational Astrophysics Centre, University of KwaZulu-Natal, Durban 4000, South Africa

⁵University of Chinese Academy of Sciences, Beijing, 100049, China

16 April 2020

ABSTRACT

We present results of HI absorption experiment done using the Giant Metrewave Radio Telescope (GMRT) towards 27 low- and intermediate-luminosity ($P_{1.4\text{GHz}} \sim 10^{23}\text{--}10^{26}$ W Hz⁻¹) radio active galactic nuclei (AGN), classified as either low excitation radio galaxies (LERGs) or high excitation radio galaxies (HERGs) and with *WISE* colour $W2[4.6\ \mu\text{m}]-W3[12\ \mu\text{m}] > 2$. We report HI absorption detection towards seven radio AGNs, six of which are new. Combined with other sources from literature classified as LERGs or HERGs, we confirm our earlier result that compact radio AGNs with *WISE* colour $W2-W3 > 2$ have higher detection rates compared to those with $W2-W3 < 2$. We find that HI absorption detection rate is higher for HERGs ($37.0_{-11.5}^{+15.8}$ per cent) compared to LERGs ($22.0_{-3.4}^{+3.9}$ per cent), mainly due to a larger fraction of HERGs being gas and dust rich with a younger stellar population compared to LERGs. However, for similar compact radio structures and host galaxies with *WISE* colours $W2-W3 > 2$, we don't find any significant difference in detection rates of two types of AGNs implying detection of HI gas may not necessarily mean high excitation mode AGN. We further analysed the kinematics towards these sources. We find that while LERGs show a wide range in the shift of centroid velocities (~ -479 to $+356$ km s⁻¹) relative to the optical systemic velocity, most of the HERGs have centroid velocity shift less than 200 km s⁻¹, possibly due to differences in jet-interstellar medium interaction.

Key words: galaxies: active – galaxies: general – galaxies: nuclei – infrared: galaxies – radio lines: galaxies – radio continuum: galaxies

1 INTRODUCTION

Almost all massive galaxies with a bulge have a supermassive black hole (SMBH) present at their centres (Kormendy & Ho 2013), which is a key component of Active Galactic Nuclei (AGN) models. However, triggering of AGN activity is not limited only to the presence of a SMBH. It also depends on the fueling mechanisms, which are found to be different according to the different types of accretion modes. In terms of Eddington accretion rate, it can be broadly classified into hyper-accretion or super Eddington accretion (Abramowicz et al. 1989); thin disk or radiatively efficient mode characterised by accretion of cold gas and a high accretion rate (Shakura & Sunyaev 1973; Novikov & Thorne 1973); and hot accretion or radiatively inefficient mode, characterised by the accretion

of hot gas and a low accretion rate (Narayan & Yi 1994, 1995; Yuan & Narayan 2014). AGNs with cold accretion modes are known to be efficiently fueled by cold interstellar medium (ISM) gas and have geometrically thin and optically thick accretion disks, surrounded by a torus of dust and cold molecular/atomic gas. Due to the presence of strong optical emission lines, these AGNs are also known as high-excitation mode AGNs (Buttiglione et al. 2010). These AGNs are also known as radiative mode AGNs as they emit efficiently radiative power across the whole electromagnetic spectrum. Based upon the orientation of torus with respect to the observer's line of sight to the central AGN, these systems are classified into Type 2 (obscured) and Type 1 (unobscured) AGNs. Obscured AGNs with the presence of dusty torus can be probed with the help of mid-IR, X-ray and radio data (Mateos et al. 2013; Mateos 2014; Mingo et al. 2016; Hickox & Alexander 2018). Different selection criteria based on all-sky mid-IR *Wide-*

* yogesh.chandola@pmo.ac.cn, yogesh.chandola@gmail.com

Field Infrared Survey Explorer (WISE; Wright et al. 2010) colour-colour diagram W1[3.4 μm]-W2[4.6 μm] vs W2[4.6 μm]-W3[12 μm] have been discussed in the literature to identify high accretion mode obscured AGNs (Donoso et al. 2009; Stern et al. 2012; Donoso et al. 2012; Yan et al. 2013; Gürkan et al. 2014, 2015; Kauffmann 2018a,b). However, it is worth noting that some amount of obscuration can be due to dust in host galaxy ISM and edge-on orientation of host galaxies. Triggering of nuclear activity in high-excitation mode AGNs is generally considered to be through mergers and interactions; the evidence for which reduces with radio power (Pierce et al. 2019). On the other hand, hot accretion mode AGNs are fueled by the cooling of hot halo gas (Narayan & Yi 1994, 1995; Yuan & Narayan 2014). In these systems, the accretion disk is geometrically thick and optically thin with no torus surrounding it (Narayan & Yi 1994, 1995; Yuan & Narayan 2014). These sources are also referred to as jet-mode AGNs (Heckman & Best 2014).

Nearly 10-20 per cent of all types of AGNs are known to show radio activity in the form of jets extending from parsec to megaparsec scales. Triggering of radio AGN activity may depend on their black hole mass and spin along with the accretion modes and nearby environment of hosts (Heckman & Best 2014). Radio AGNs with high-excitation emission lines and cold accretion mode are termed as High Excitation Radio Galaxies (HERGs) while those with weak emission lines are known as Low Excitation Radio Galaxies (LERGs). In the nearby Universe ($z < 0.3$), LERGs dominate at low ($P_{1.4\text{GHz}} \sim 10^{23} - 10^{24.3} \text{ WHz}^{-1}$) and intermediate radio powers ($P_{1.4\text{GHz}} \sim 10^{24.3} - 10^{26} \text{ WHz}^{-1}$) while HERGs are dominant at high radio powers ($P_{1.4\text{GHz}} > 10^{26} \text{ WHz}^{-1}$) (Best & Heckman 2012b). LERGs are hosted by massive early-type galaxies with higher SMBH mass as compared to HERGs. LERG hosts have an older stellar population and lower accretion rates as compared to HERGs (Whittam et al. 2018). Williams et al. (2018) studied properties of intermediate to high redshift LERG and HERG hosts, to find that LERG luminosity function shows negative evolution with increasing redshift ($z \sim 0.5-2$) implying decrease in LERG population and HERG as a dominant population at higher redshifts for all values of radio power. This is consistent with the scenario of AGN-host galaxy co-evolution with redshift. Mechanical feedback from radio AGNs is one of the important factors, which can significantly impact this co-evolution. Whittam et al. (2018) find $\sim 10\%$ of accretion power is released as mechanical feedback via radio jets for almost all sources in their sample irrespective of accretion modes.

In radio AGNs, evidence of feedback has been found as outflows of ionized as well as neutral atomic and molecular gas (e.g. PKS1549-79, Tadhunter et al. 2001; 3C305, Morganti et al. 2005; IC5063, Morganti et al. 2007). In the ultra-luminous infra-red galaxy (ULIRG) 4C12.50, Morganti et al. (2013) reported ongoing parsec scale atomic hydrogen outflow due to jet-cloud interaction coinciding with molecular CO outflow (Dasyra & Combes 2012). In some cases, evidence of jet-cloud interactions has been found in the form of largely blueshifted HI absorption profiles with widths up to several 1000 km s^{-1} (Mahony et al. 2013; Aditya & Kanekar 2018). Outflowing gas in different phases, especially the cold gas, may have a significant effect on star formation. However, how this may affect the star-formation

of host galaxies is still a subject of debate (Harrison 2017). Some studies suggest that AGN outflows deplete the cold gas reservoir in host galaxies, leading to suppressed star-formation (Lehnert et al. 2011; Ciccone et al. 2014). Massive outflow of molecular gas $\dot{M} \approx 110 M_{\odot} \text{ yr}^{-1}$ was detected in NGC1266 but only $2 M_{\odot} \text{ yr}^{-1}$ could escape the galaxy (Alatalo et al. 2015). In this galaxy, star formation rate was found to be suppressed by a factor of ≈ 50 (Kennicutt-Schmidt law) (Kennicutt 1998) compared with a normal star-forming galaxy, possibly due to mechanical interaction. However, in the galaxy Mrk 231, despite a massive outflow of molecular gas, star-formation efficiency is consistent with the Kennicutt-Schmidt law (Alatalo 2015). Also, the jet-ISM interaction may have an important role in determining the evolutionary path (Kunert-Bajraszewska et al. 2010; An & Baan 2012) and structures of radio sources (Gopal-Krishna & Wiita 2000).

HI 21-cm absorption towards radio AGNs is a useful technique which has been used to probe the presence of HI gas in the circumnuclear environment of these sources (Vermeulen et al. 2003; Beswick et al. 2004; Gupta et al. 2006; Chandola et al. 2010, 2011, 2012, 2013; Salter et al. 2010; Allison et al. 2015; Maccagni et al. 2017; Aditya et al. 2017; Aditya & Kanekar 2018; Glowacki et al. 2019; Grasha et al. 2019). Studying cold HI gas and its kinematics in the host galaxies and nearby environment of radio AGNs is useful for understanding the fueling and triggering of radio AGN activity in these sources. It is also useful for understanding the feedback effect from central AGN that may affect the star-formation activity in the host galaxy. Several intrinsic physical properties, as well as geometrical factors, which affect the probability of detecting HI absorption, have been discussed in the literature. These factors include the size of radio structure, radio power, central AGN characteristics and properties of host galaxy interstellar medium (please see recent review by Morganti & Oosterloo 2018).

In an earlier paper, we explored the dependence of HI absorption properties of the sources on HERGs/LERGs and hence on the accretion mode, source size, and nature of the host galaxy as reflected by the WISE infrared colours (Chandola & Saikia 2017). We considered the sample of 100 sources observed uniformly by Geréb et al. (2015) and the classification into high-excitation and low-excitation radio galaxies done by Best & Heckman (2012b). We found HI detection rates have a significant dependence on WISE W2-W3 colours with those with $W2-W3 > 2$ and compact radio structures having detection rates ~ 70 per cent. We also found a trend, which shows HERGs have higher HI absorption detection rates as compared to LERGs as most of them are with $W2-W3 > 2$. However, for all HERGs and LERGs with $W2-W3 > 2$, there was no significant difference in their detection rates. We also reported a trend that HI absorption lines associated with HERGs have a narrower range in shift with respect to the velocity corresponding to the red-shift derived from optical emission lines as compared to LERGs. Our study was limited by a small number of 11 HERGs because this low and intermediate radio-power ($P_{1.4\text{GHz}} \sim 10^{23} - 10^{26} \text{ WHz}^{-1}$) sample was dominated by LERGs. In this paper, we extend our study to a larger number of low- and intermediate-luminosity HERGs from our observations with the Giant Metrewave Radio Telescope (GMRT). In addition,

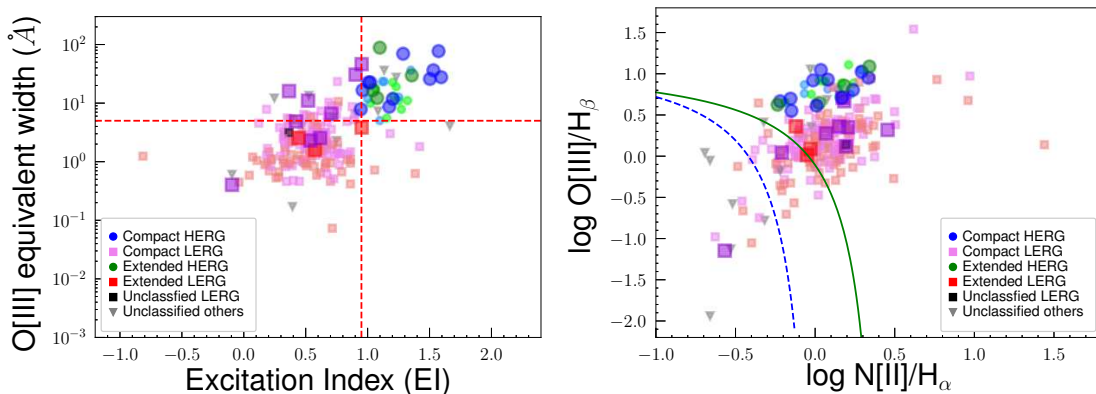


Figure 1. **Left:** O[III] equivalent width versus excitation index (for 211 sources with all six emission lines used to calculate excitation index). The “excitation index” has been defined by Buttiglione et al. (2010) as $EI = \log_{10}([OIII]/H\beta) - \frac{1}{3} [\log_{10}([NII]/H\alpha) + \log_{10}([SII]/H\alpha) + \log_{10}([OI]/H\alpha)]$. Compact and extended HERGs are shown with blue and green circles respectively, while compact, extended and structurally unclassified LERGs are shown with violet, red and black colored squares respectively. Unclassified sources are shown as grey downward triangles. Sources observed with the GMRT are shown with larger symbols with darker shades. Smaller symbols with lighter shades represent sources from Maccagni et al. (2017). While the horizontal line is for O [III] equivalent width = 5 Å, the vertical line depicts EI = 0.95. **Right:** log O [III]/H_β versus log N [II]/H_α for 238 sources which have the required spectral information. While the dashed blue curve is the Kauffmann et al. (2003) dividing line between star-forming (SF) and composite (SF+AGN) galaxies, the solid green curve shows the Kewley et al. (2001, 2006) dividing line between AGNs and composite galaxies. Symbols have the same meaning as in the left plot.

we also consider sources from the literature to compare with LERGs, to explore differences in the kinematics of HI gas in the hosts of these two types of AGNs.

This paper is organized as follows. In Section 2, we describe the sample. In Section 3, we explain the observational details and data reduction method. In Section 4, we report the results from our study and discuss these in the Section 5. We summarise our findings in section 6. In this paper, we adopt a cosmological model with $H_0=70 \text{ km s}^{-1} \text{ Mpc}^{-1}$, $\Omega_m=0.3$ and $\Omega_\Lambda=0.7$. *WISE* colours in this paper are in Vega magnitude.

2 SAMPLE

From the sample of radio AGNs compiled by Best & Heckman (2012a,b) using the SDSS optical spectroscopic data (DR7; Abazajian et al. 2009) and the *Faint Images of the Radio Sky at Twenty Centimeters survey* (FIRST; Becker et al. 1995) and *NRAO VLA Sky Survey* (NVSS; Condon et al. 1998), we compiled a sample for HI absorption observations, which satisfy the following criteria: $S(1400 \text{ MHz}) > 80 \text{ mJy}$, redshift $z < 0.2$, *WISE* colour $W2-W3 > 2$ and classified as either a LERG or HERG. *WISE* colour $W2-W3 > 2$ selection was done in order to increase the chances of HI absorption detection. This resulted in a sample of 71 sources, of which 29 were HERGs and 42 LERGs. With the allocated time we observed 30 sources with the Giant Metrewave Radio Telescope (GMRT). Of these 30, 3 were found later to have significant redshift uncertainties and have not been used in this analysis. Of the remaining 27 sources listed in Table 1, 12 have been classified as LERGs and 15 as HERGs by Best & Heckman (2012b). Of these 27, 7 sources, 4 LERGs and 3 HERGs, have baseline ripples in the spectra, and are not used in our final analysis (also see Section 4).

In addition to the sources observed with the GMRT, we also considered 219 radio AGNs from a larger sample studied in HI absorption by Maccagni et al. (2017) using Westerbork Synthesis Radio Telescope (WSRT) and common with the sample of Best & Heckman (2012b) for this study. Of these 219 radio AGNs, 189 are classified as LERGs and 15 as HERGs by Best & Heckman (2012b) while the remaining 15 are unclassified. In this sample, 5 sources, all LERGs, (J0816+3804, J0906+4636, J1400+5216, J1435+5051 and J1447+4047) are common with our GMRT observed sample in Table 1. By combining the two samples, we have now a sample of 241 low- and intermediate- radio power ($P_{1.4\text{GHz}} \sim 10^{22.5}-10^{26.2} \text{ WHz}^{-1}$) AGNs, which include 196 LERGs and 30 HERGs, to study the HI absorption properties. Of these 241 sources, we have shown in Fig. 1 the classification of 211 radio AGNs by Best & Heckman (2012b) in O[III] equivalent width vs. excitation index plot and 238 radio AGNs in BPT (Baldwin et al. 1981) diagram using the SDSS spectral line catalog data¹ from Max Planck Institute for Astrophysics and John Hopkins University group (hereafter MPA-JHU; Brinchmann et al. 2004). The remaining three sources, J1030+4113, J1325+4920 and J1516+2919, have no detection of H_α emission line in SDSS DR7 and hence not shown in these plots. Of these 3, J1030+4113 and J1325+4920 are LERGs while J1516+2919 is unclassified.

Of the five sources which are in common, all of which are LERGs, J0816+3804, J1400+5216 and J1447+4047 are undetected in both our GMRT observations as well as in the sample of Maccagni et al. (2017). The present observations of J0906+4636 were affected by a bandpass ripple while earlier Chandola et al. (2011) reported a detection and Geréb et al. (2015) a non-detection. For the fifth source J1435+5051 both Chandola et al. (2011) and the present

¹ <http://wwwmpa.mpa-garching.mpg.de/SDSS/DR7/>

Table 1. Radio sources observed with the GMRT.

(1) Source name	(2) R.A. (J2000)	(3) Dec (J2000)	(4) Redshift	(5) LERG/HERG	(6) C/E	(7) Radio spectral class [†]	(8) $\log P_{1.4\text{GHz}}^*$ W Hz^{-1}
J0028+0055	00:28:33.454	+00:55:10.95	0.10429	LERG	C	CSS	24.63
J0813+0734	08:13:23.752	+07:34:05.69	0.11239	LERG	C	CSS	25.26
J0816+3804	08:16:01.822	+38:04:14.30	0.17275	LERG	E	–	25.26
J0832+1832	08:32:16.042	+18:32:12.08	0.15411	HERG	C	GPS/CFS?	25.64
J0853+0927	08:53:23.429	+09:27:44.33	0.11569	HERG	C	CFS	24.52
J0906+4636	09:06:15.544	+46:36:19.04	0.0847	LERG	C	CFS	24.70
J0912+5320	09:12:01.404	+53:20:35.36	0.10173	HERG	C	CFS	24.45
J1056+1419	10:56:38.839	+14:19:30.39	0.08127	LERG	C	CSS	24.43
J1058+5628	10:58:37.724	+56:28:11.26	0.14324	LERG	C	CFS	25.12
J1107+1825	11:07:01.191	+18:25:48.80	0.17856	HERG	C	CSS	25.04
J1110+2131	11:10:20.462	+21:31:45.82	0.13461	HERG	C	CSS	25.06
J1156+2632	11:56:54.672	+26:32:32.38	0.15625	HERG	C	CFS	24.69
J1217–0337	12:17:55.297	–03:37:23.16	0.18229	HERG	E	–	25.23
J1328+1738	13:28:59.269	+17:38:42.31	0.18035	HERG	C	CFS	25.19
J1341+5344	13:41:34.847	+53:44:43.82	0.14094	HERG	E	–	25.70
J1350+0940	13:50:22.142	+09:40:10.64	0.13255	LERG	C	GPS/CFS?	24.98
J1352–0156	13:52:23.470	–01:56:48.32	0.16694	HERG	E	–	25.56
J1400+5216	14:00:51.581	+52:16:06.55	0.11789	LERG	C	CSS	24.74
J1410+1438	14:10:28.055	+14:38:40.22	0.14419	LERG	E	–	25.34
J1435+5051	14:35:21.664	+50:51:22.16	0.09969	LERG	C	CFS	24.51
J1447+4047	14:47:12.766	+40:47:45.02	0.19515	LERG	E	–	25.58
J1449+4221	14:49:20.710	+42:21:01.39	0.17862	HERG	C	CFS	24.93
J1534+2330	15:34:57.247	+23:30:11.48	0.0184	LERG	C	CFS	23.40
J1538+5525	15:38:36.083	+55:25:41.39	0.19117	HERG	C	CSS	25.32
J1543+0235	15:43:17.401	+02:35:52.04	0.18793	HERG	E	–	25.58
J1559+5330	15:59:27.661	+53:30:53.52	0.17918	HERG	C	CSS	25.09
J2133–0712	21:33:33.322	–07:12:49.30	0.08654	HERG	C	CSS	24.54

Column 1: source name; column 2: right ascension (J2000); column 3: declination (J2000); column 4: redshift; column 5: LERG and HERG classification based on [Best & Heckman \(2012b\)](#); column 6: radio structural classification as compact (C) and extended (E), sources with $\lesssim 20$ kpc in linear projected sizes are classified as compact and larger ones as extended; column 7: radio spectral class; column 8: logarithm of luminosity at 1.4 GHz in units of W Hz^{-1} .

[†]: Using the radio flux densities obtained from ViZieR photometry viewer (<http://vizier.u-strasbg.fr/vizier/sed/>). CFS: Compact Flat Spectrum; CSS: Compact Steep Spectrum; GPS: Gigahertz Peaked Spectrum. Sources with spectral index (α) ≤ 0.5 are classified as flat spectrum sources while sources with $\alpha > 0.5$ are classified as steep spectrum sources, where $S_\nu \propto \nu^{-\alpha}$.

*: Using integrated flux densities listed in Table 3.

Table 2. Observational details of the search for associated HI absorption.

(1) Source name	(2) Ob. frequency (MHz)	(3) Flux Cal.	(4) Phase Cal.	(5) Ob. Date	(6) Hours
J0028+0055	1286.26	3C48	0022+002	November 10, 2016	4
J0813+0734	1276.90	3C147	0745+101	November 11, 2016	3
J0816+3804	1211.18	3C48,3C147	0741+312	November 12, 2016	4
J0832+1832	1230.74	3C147	0842+185	May 15, 2016	3
J0853+0927	1273.12	3C48, 3C286	0842+185	November 01, 2016	6
J0906+4636	1309.49	3C147	0713+438	December 09, 2016	4
J0912+5320	1289.25	3C147	0614+607	November 02, 2016	5
J1056+1419	1313.65	3C147, 3C286	1120+143	December 02, 2016	4
J1058+5628	1242.44	3C147	1035+564	December 02, 2016	4
J1107+1825	1205.20	3C48	1120+143	May 29, 2016	4
J1110+2131	1251.89	3C286	1120+143	July 31, 2016	3
J1156+2632	1228.46	3C286	1221+282	November 13, 2016	6
J1217–0337	1201.40	3C147, 3C286	1150–003	July 09, 2016	4
J1328+1738	1203.38	3C286	1347+122	December 18, 2016	5
J1341+5344	1244.94	3C286	1400+621	November 13, 2016	3
J1350+0940	1254.17	3C286	1445+099	November 15, 2016	3
J1352–0156	1217.21	3C286	1445+099	July 09, 2016	3
J1400+5216	1270.61	3C147, 3C286	1400+621	November 12, 2016	4
J1410+1438	1241.41	3C286	1445+099	November 14, 2016	3
J1435+5051	1291.64	3C286	1438+621	December 17, 2016	4
J1447+4047	1188.47	3C286	1602+334	December 18, 2016	3
J1449+4221	1205.14	3C286	1602+334	September 01, 2016	4
J1534+2330	1394.74	3C286	1609+266	December 20, 2016	3
J1538+5525	1192.46	3C286	1438+621	July 09, 2016	4
J1543+0235	1195.70	3C286	1445+099	June 06, 2016	3
J1559+5330	1204.57	3C286	1438+621	June 16–17, 2016	4
J2133–0712	1307.27	3C48	2136+006	May 13, 2016	4

Column 1: source name; column 2: central line frequency used for observation in MHz; column 3: flux density/bandpass calibrator; column 4: Phase calibrator; column 5: date of observation; column 6: total observation time in hours.

Table 3. Results of the search for associated HI absorption.

(1)	(2)	(3)	(4)	(5)	(6)	(7)	(8)	(9)	(10)	(11)	(12)	(13)
Source name	Vel. res.	Beam size	S_{int}	S_{peak}	ΔS_{rms}	τ_{rms}	$\int \tau dv$	$N(\text{HI})$	No. Gauss	Velo. shift	FWHM	τ_{peak}
	km s^{-1}	" \times "", P.A. ($^{\circ}$)	mJy	mJy/b	mJy/b		km s^{-1}	10^{20} cm^{-2}		km s^{-1}	km s^{-1}	
J0028+0055	7.67	2.69 \times 2.23, 80.56	183.9	124.1	1.09	0.009	<1.2	<2.1	0			
J0813+0734	7.74	2.63 \times 1.68, 57.89	676.6	547.3	–	–	–	–	–			
J0816+3804	8.18	2.60 \times 1.55, 25.40	277.8	21.6	3.51	0.166	<22.8	< 41.5	0			
J0832+1832	8.02	2.35 \times 1.64, 67.88	823.0	758.4	–	–	–	–	–			
J0853+0927	7.73	2.08 \times 1.55, 51.98	111.7	101.4	1.34	0.01	10.5 \pm 0.8	19.0 \pm 1.4	1	–351.1 \pm 40.1	144.2 \pm 68.5	0.022 \pm 0.005
									2	–206.2 \pm 15.9	132.9 \pm 25.9	0.050 \pm 0.007
J0906+4636	8.19	2.91 \times 1.82, 38.67	312.8	308.6	–	–	–	–	–			
J0912+5320	7.65	2.82 \times 1.67, 67.77	121.2	121.7	1.15	0.009	1.8 \pm 0.3	3.4 \pm 0.5	1	25.6 \pm 3.2	41.2 \pm 7.4	0.042 \pm 0.007
J1056+1419	7.5	2.40 \times 1.72, 59.33	185.8	166.7	2.04	0.012	7.0 \pm 0.8	12.8 \pm 1.4	1	–2.7 \pm 6.0	161.9 \pm 15.0	0.036 \pm 0.003
									2	158.2 \pm 4.0	32.3 \pm 9.6	0.024 \pm 0.006
J1058+5628	7.9	3.22 \times 1.57, 66.09	270.7	260.5	–	–	–	–	–			
J1107+1825	8.19	2.79 \times 1.84, 89.97	156.4	128.6	–	–	–	–	–			
J1110+2131	7.91	2.22 \times 2.05, 27.99	285.5	270.6	1.18	0.004	<0.6	<1.1	0			
J1156+2632	8.0	2.15 \times 1.72, –87.73	86.35	84.8	1.27	0.015	<2.0	<3.7	0			
J1217–0337	8.23	2.48 \times 2.15, –5.39	235.8	159.8	1.52	0.01	<1.3	<2.4	0			
J1328+1738	8.19	2.21 \times 1.71, 77.22	205.4	193.1	1.76	0.009	<1.3	<2.4	0			
J1341+5344	7.92	3.34 \times 1.69, 63.5	1260.2	14.1	1.69	0.124	<16.7	<30.4	0			
J1350+0940	7.85	2.85 \times 1.88, 86.04	239.2	235.9	–	–	–	–	–			
J1352–0156	8.15	3.44 \times 1.96, 54.12	616.0	361.2	1.63	0.005	5.8 \pm 0.4	10.6 \pm 0.7	1	44.0 \pm 13.9	299.6 \pm 27.8	0.013 \pm 0.001
									2	146.4 \pm 1.3	38.5 \pm 1.5	0.041 \pm 0.003
J1400+5216	7.76	3.08 \times 1.36, 54.79	179.3	166.6	2.82	0.017	<2.3	<4.1	0			
J1410+1438	7.96	3.74 \times 1.93, 87.42	480.4	125.6	1.31	0.01	<1.4	<2.6	0			
J1435+5051	7.65	2.77 \times 1.61, 55.47	147.3	147.0	1.15	0.008	<1.0	<1.9	0			
J1447+4047	8.3	2.48 \times 1.84, 19.73	456.7	44.5	1.35	0.031	<4.2	<7.7	0			
J1449+4221	8.2	2.57 \times 2.27, –63.0	111.0	111.2	1.33	0.012	<1.7	<3.0	0			
J1534+2330	7.06	2.55 \times 1.81, 69.46	349.3	277.1	1.21	0.004	89.4 \pm 0.5	163.0 \pm 0.9	1	–325.9 \pm 14.3	139.3 \pm 25.3	0.024 \pm 0.003
									2	–219.5 \pm 3.9	85.8 \pm 11.5	0.046 \pm 0.008
									3	–97.4 \pm 0.7	24.8 \pm 2.0	0.057 \pm 0.004
									4	–65.4 \pm 1.6	255.6 \pm 6.5	0.285 \pm 0.002
									5	77.0 \pm 0.8	17.8 \pm 2.0	0.045 \pm 0.004
									6	156.0 \pm 11.8	121.2 \pm 27.6	0.014 \pm 0.003
J1538+5525	8.23	3.06 \times 1.82, 44.2	259.6	182.4	0.84	0.005	2.0 \pm 0.3	3.6 \pm 0.6	1	–105.3 \pm 2.3	18.3 \pm 5.9	0.021 \pm 0.006
									2	–48.8 \pm 23.0	186.0 \pm 48.4	0.008 \pm 0.002
J1543+0235	8.28	3.12 \times 2.35, –82.92	495.2	297.2	–	–	–	–	–			
J1559+5330	8.21	3.22 \times 1.64, 11.53	177.7	168.2	3.06	0.01	<1.4	<2.6	0			
J2133–0712	14.85	2.59 \times 2.11, 37.1	213.7	211.3	0.64	0.003	5.5 \pm 0.1	10.1 \pm 0.3	1	50.6 \pm 0.5	51.8 \pm 1.2	0.119 \pm 0.002

Column 1: source name; column 2: velocity resolution; column 3: spatial resolution in arcseconds and position angle (P.A.) in degrees; column 4: integrated flux density in mJy; column 5: Peak flux density in mJy/beam for the continuum image made using line free channels; column 6: r.m.s.in line free channels; column 7: r.m.s in optical depth for line free channels ; column 8: Integrated optical depth, and column 9: HI column density in units of 10^{20} cm^{-2} , assuming $T_{\text{S}}=100 \text{ K}$ and a covering factor, f_c of unity; upper limits are 3σ values, assuming FWHM $\Delta v=100 \text{ km s}^{-1}$; column 10: No. of Gaussian component; columns 11 to 13: fit parameters of Gaussian profiles, velocity shift w.r.t. systemic velocity, Full Width Half Maximum and peak optical depth.

GMRT observations do not find a detection from two independent observations, while [Maccagni et al. \(2017\)](#) report a detection from a somewhat noisier spectrum compared with most of their sources. Therefore while considering the [Maccagni et al. \(2017\)](#) and GMRT samples separately we have adopted the results for these two sources as reported by the authors in the respective samples, but have left them out from the combined sample. A further set of observations is required to clarify the discrepancy in the two sources. This does not at all affect the results presented in this paper. Hence, for HI analysis, after excluding these two sources and 6 other sources affected by radio frequency interference (RFI) or baseline ripples in our GMRT sample, we have 233 radio sources including 191 LERGs and 27 HERGs for combined sample. The remaining 15 are unclassified as mentioned earlier. This sample henceforth be referred to as the ‘combined sample’. In this sample, we have around two and a half times the number of LERGs (80) and HERGs (11) compared to our previous work ([Chandola & Saikia 2017](#)), which help us to understand the HI absorption properties in both types of AGNs better. However, while giving HI statistics separately for [Maccagni et al. \(2017\)](#) and GMRT observed samples, we use 219 sources from their sample, and all 20 sources with good spectra from the GMRT observed sample.

3 OBSERVATION AND DATA REDUCTION

HI 21cm absorption experiments were done towards these sources with the GMRT during May-December 2016. During these observations, the GMRT full array was used in total intensity mode and base-band bandwidth of 16 MHz divided into 512 channels (except for J2133-0712 where 256 channels were used). This resulted in velocity spectral resolution of $\sim 8 \text{ km s}^{-1}$, except for J2133-0712 where it is $\sim 15 \text{ km s}^{-1}$. Observational details for these sources are listed in Table 2. After every 40 minutes of observing time on the target source, phase calibrator was observed for 5 minutes. Flux density or bandpass calibrators were observed for 10-15 minutes after every 3-4 hours of observations.

Data were reduced mainly using the NRAO AIPS package. Initially, data reduction was done for a single channel. Bad data due to RFI and bad antennas were flagged before any calibration using TVFLG, UVFLG. Phase and gain calibration solutions and bandpass calibration solutions were determined using the task CALIB and the task BPASS respectively. Bad data were iteratively flagged until satisfactory gain solutions were obtained. Then the target source data were split from the multi-source data cube after applying the bandpass and gain solutions. The target source data were examined and bad data flagged before imaging using the task IMAGR. After a few rounds of self-calibration, RFI was removed from the spectral line *uv* datacube using RFI removing software AOFLAGGER ([Offringa 2010](#)), except for extended sources where it was done manually using AIPS task SPFLG. Next, the final continuum images were made from line free channels. The continuum data were then subtracted from the spectral line *uv* datacube using tasks UVSUB and UVLIN. Task CVEL was used to correct for the motion of the Earth’s rotation. Finally, the HI absorption spectra were extracted from the HI dirty image cube

against the pixels corresponding to the peak flux densities towards the central regions of target source images.

4 RESULTS

In this Section, we report HI absorption properties of our sample. Of the 27 sources, we have obtained reliable spectra towards 20 sources. Of these 20 sources, we report 7 detections ($\sim 35\%$ detection rate), of which 6 detections are new. The HI absorption profiles and Gaussian fits to these are shown in Fig. 2. Of the 7 detections, 2 HI absorption profiles could be fitted with a single Gaussian component, 4 HI absorption profiles with two Gaussian components and one, J1534+2330, with 6 Gaussian components. HI absorption towards J1534+2330 or Arp 220 has been also reported in earlier studies ([Mirabel 1982](#); [Garwood et al. 1987](#); [Mundell et al. 2001](#); [Allison et al. 2014](#)). HI absorption towards Arp 220 is due to two counterrotating HI disks and bridge of gas connecting them ([Mundell et al. 2001](#)). We have listed the Gaussian parameters from HI absorption profiles and values of column densities in Table 3. HI profiles towards 13 sources with non-detection are shown in Fig. 3. Of the 27 sources, 7 have been affected with ripples (Fig. 4) and are not included in our analysis. We have also written notes on individual sources in the Appendix. While Gaussian models of HI absorption profiles are used to parameterize the physical conditions and individual components in these absorbers, we also obtain Busy fit parameters ([Westmeier et al. 2014](#)) to describe the average characteristics of the profiles. The Busy fit parameters are listed in Table 4. For single component HI absorption profiles, there is no significant difference in velocities for the Gaussian component and centroid of Busy function relative to optical systemic velocity. However, in case of multiple components, centroid velocity of Busy function relative to optical systemic velocity may miss extreme redshifted or blueshifted components. For example, in case of J1534+2330, the velocity at the centroid of Busy function relative to optical redshift is $\sim -78 \text{ km s}^{-1}$ but the Gaussian component with maximum blueshift has a velocity of $\sim -326 \text{ km s}^{-1}$ relative to optical systemic velocity. Hence for our analysis, in order to get an idea of extreme blueshifted velocity from Busy function, we estimated the blueshifted velocity at FW20 relative to optical systemic velocity as, $-V_{\text{FW20}} = V_{\text{centroid}} - \text{FW20}/2$, where V_{centroid} and FW20 are the velocity at centroid relative to optical systemic velocity and full width at twenty per cent of maximum in km s^{-1} , respectively. We mark both, V_{centroid} and $-V_{\text{FW20}}$ with green and blue dashed vertical lines respectively in Fig 2.

Optical depths (τ) have been estimated from the line-to-continuum ratio by using the equation

$$\tau = -\ln\left(1 - \frac{\Delta I}{f_c I_c}\right), \quad (1)$$

where ΔI is the absorbed flux density, I_c is the continuum flux density and f_c is the fraction of the background source covered by absorbing gas. We have assumed $f_c = 1$ for our calculations. The r.m.s noise on τ as a function of the peak flux density for our GMRT sample and [Maccagni et al.](#)

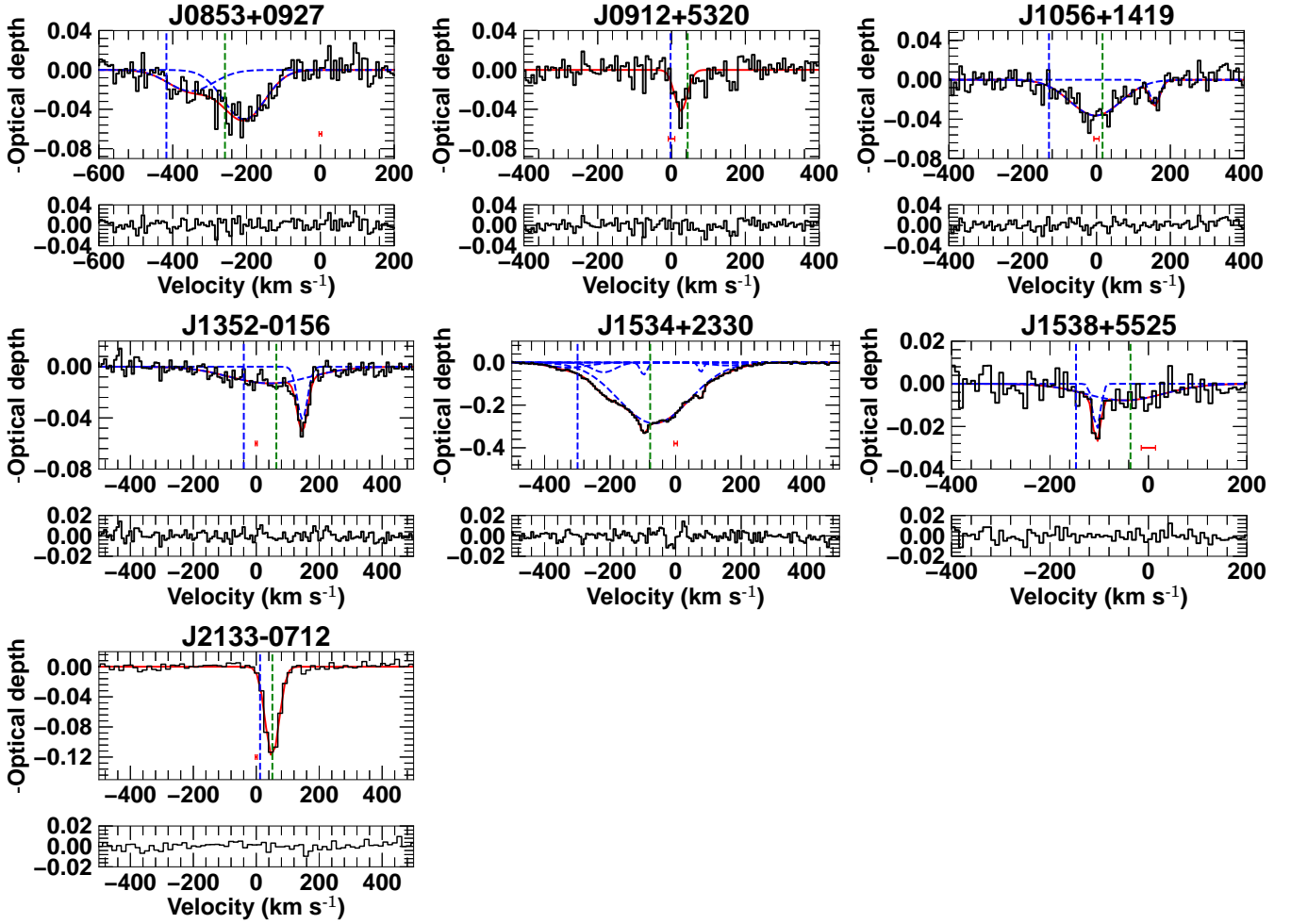


Figure 2. HI absorption profiles towards brightest pixel in sources detected with HI absorption. X-axes show velocity shift w.r.t. optical systemic velocity and Y-axes show optical depth. Zero represent the optical systemic velocity corresponding to optical redshift. Gaussian profile fit to the profiles are shown with red colour lines, where individual components are shown with blue colour dashed lines. Residuals from fit are shown at the bottom panels of each plot. Error bars in red colour at the bottom of each plot show the error in optical redshift. Green and blue dashed vertical lines show position of V_{centroid} and $-V_{\text{FW}20}$ respectively for Busy function fit.

(2017) sample² is shown in Fig 5 top panel. Since most of the sources in our sample have peak flux density > 100 mJy and in their sample < 100 mJy, the median value of τ r.m.s. achieved from our GMRT observation is 0.009 per channel as compared to 0.015 per channel for the WSRT sample. However, for a similar range of peak flux densities in both the samples ($S_{\text{peak}} = 90\text{-}300$ mJy/beam) where most (15/20) of our sources are located, our observations are slightly less sensitive (median $\tau_{\text{rms}} = 0.009$) than those of Maccagni et al. (2017) (median $\tau_{\text{rms}} = 0.007$). It is also to be noted that median velocity spectral resolution for our GMRT sample is ~ 7.9 km s⁻¹ as compared to ~ 16 km s⁻¹ in the Maccagni et al. (2017) sample.

² We used FIRST peak flux densities to estimate the optical depth for Maccagni et al. (2017) sample.

4.1 Integrated optical depth and column densities

Integrated optical depths are calculated using equation

$$\int \tau dv = 1.064 \times \tau_{\text{peak}} \times \text{FWHM}, \quad (2)$$

for a Gaussian profile. FWHM and τ_{peak} are full width at half maximum and peak optical depth, respectively obtained from the Gaussian fits. The error on integrated optical depth is estimated as $\tau_{\text{rms}} \times \delta v \times \sqrt{\text{FWZI}/\delta v}$, where δv , τ_{rms} and FWZI are velocity resolution in km s⁻¹, rms noise on optical depth and full width at zero intensity, respectively. We have assumed FWZI for Gaussian profiles to be 6σ i.e. $2.547 \times \text{FWHM}$. We also estimated 3σ upper limits for the non-detections by assuming a Gaussian profile with FWHM = 100 km s⁻¹ and using

$$\int \tau dv = 3 \times \tau_{\text{rms}} \times \delta v \times \sqrt{2.547 \times \text{FWHM}/\delta v}. \quad (3)$$

For a range of similar peak flux densities (90-300 mJy/beam) in both samples, median integrated optical

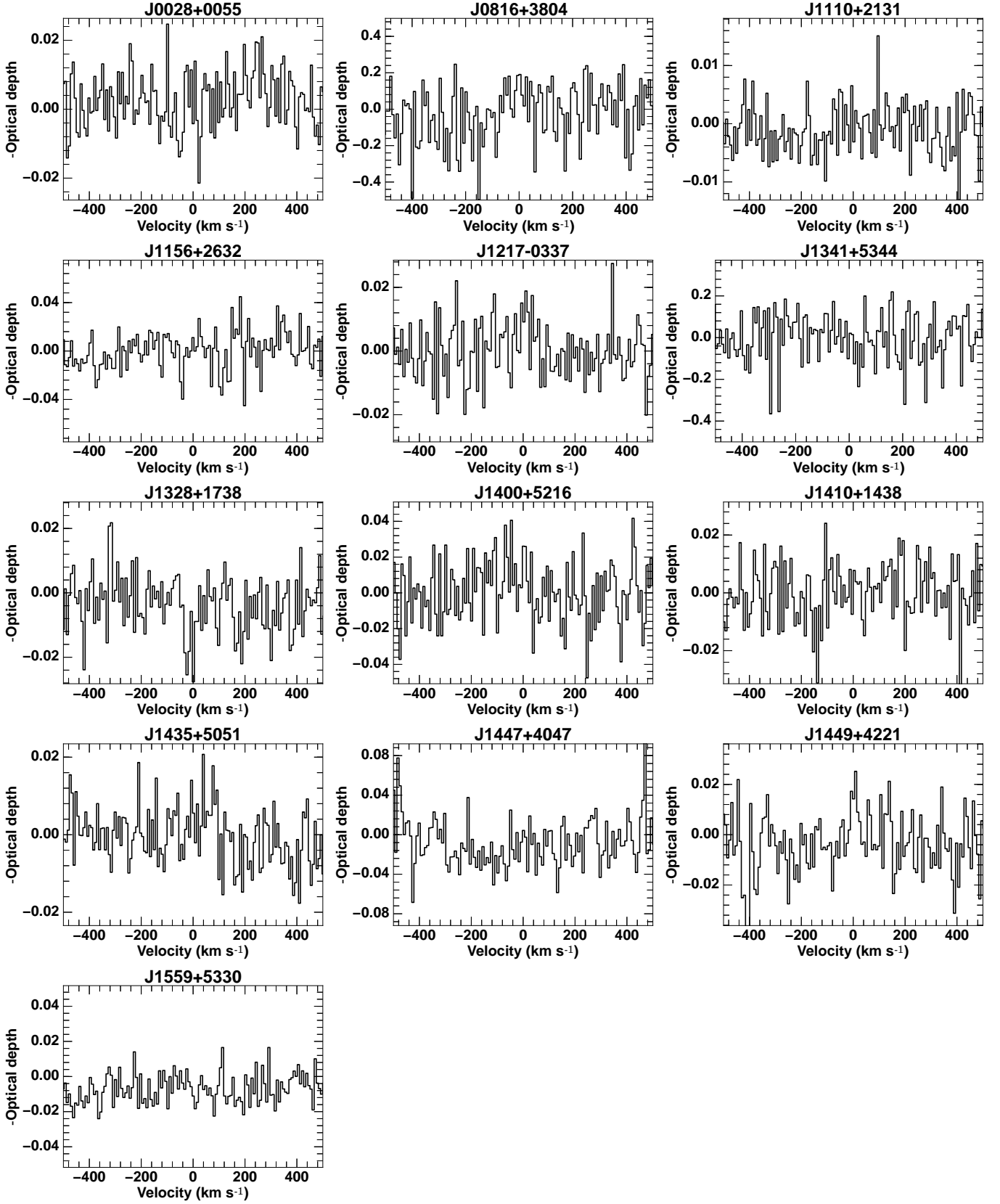


Figure 3. HI absorption profiles towards brightest pixel in sources not detected with HI absorption. X-axes show velocity shift w.r.t. optical systemic velocity and Y-axes show optical depth. Zero represent the optical systemic velocity corresponding to optical redshift.

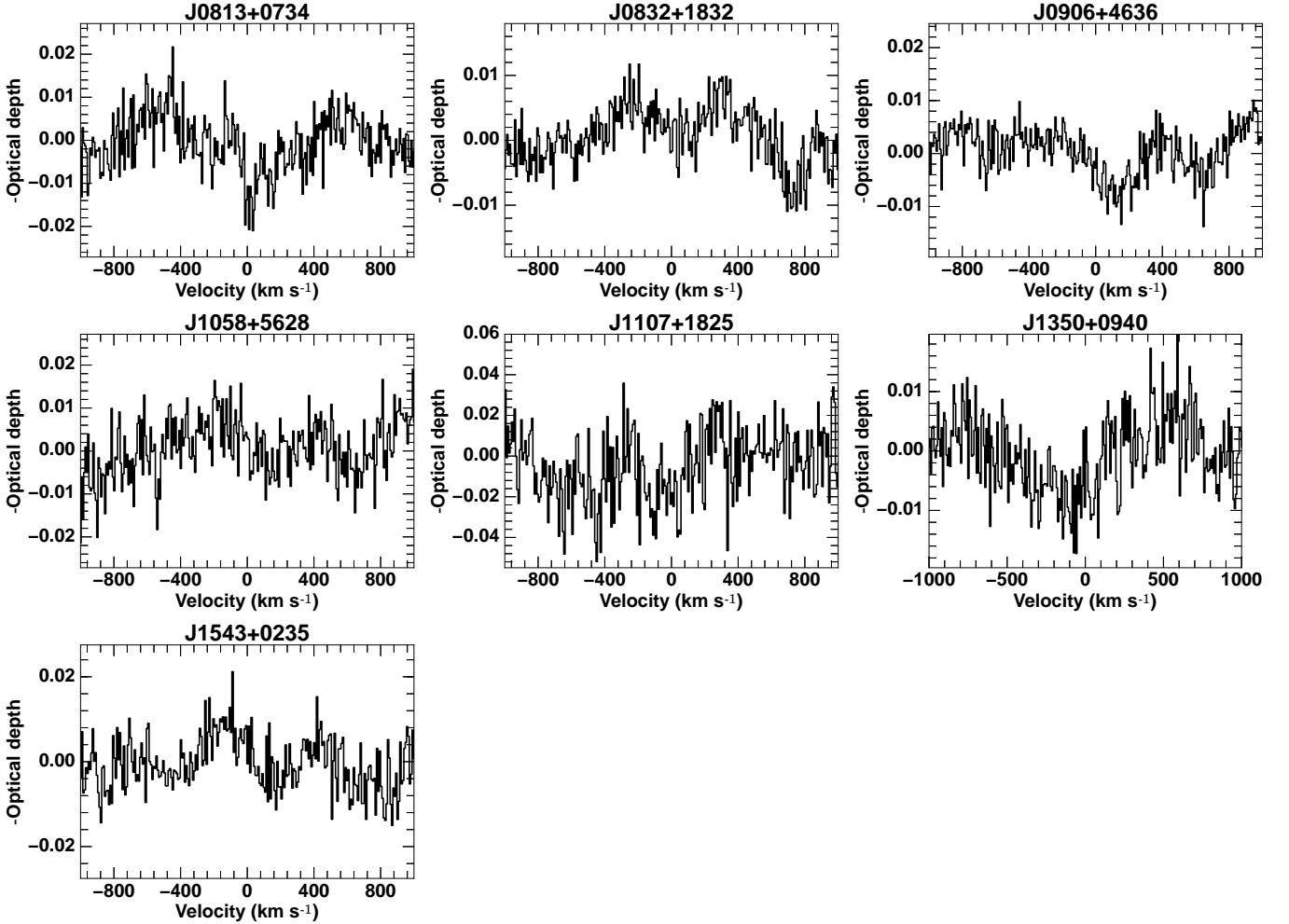


Figure 4. HI absorption profiles towards brightest pixel in sources affected with ripples. X-axes show velocity shift w.r.t. optical systemic velocity and Y-axes show optical depth. Zero represent the optical systemic velocity corresponding to optical redshift.

depth estimated for detections is 7.0 km s^{-1} , and for the non-detections the median value for the 3σ upper limit is 1.3 km s^{-1} for the GMRT sample. The corresponding values for the Maccagni et al. (2017) sample are 6.0 km s^{-1} and 1.2 km s^{-1} respectively (Fig 5 bottom).

We also estimated the HI column densities and upper limits using equations (2) and (3) in the equation (Wolfe & Burbidge 1975),

$$N(\text{HI}) = 1.823 \times 10^{18} T_s \int \tau dv, \quad (4)$$

where T_s is the spin temperature. We assume $T_s = 100 \text{ K}$. The median column density for HI absorption detection from GMRT sample is estimated to be $10.6 \times 10^{20} \text{ cm}^{-2}$. The median 3σ upper limit for HI absorption non-detections on column density is estimated to be $2.6 \times 10^{20} \text{ cm}^{-2}$. The corresponding values for the Maccagni et al. (2017) sample are $16.4 \times 10^{20} \text{ cm}^{-2}$ and $3.5 \times 10^{20} \text{ cm}^{-2}$, respectively.

In the combined GMRT and Maccagni et al. (2017) sample, the median integrated optical depths for HI detections are 8.7 km s^{-1} and 5.7 km s^{-1} for LERGs and HERGs respectively. The corresponding median column densities are

$15.9 \times 10^{20} \text{ cm}^{-2}$ and $10.4 \times 10^{20} \text{ cm}^{-2}$ for LERGs and HERGs respectively.

4.2 Detection rates

In this subsection, we present the detection rates of radio AGNs according to their classification based on accretion modes, *WISE* colours, and radio properties such as radio power and structures. We have estimated the errors on detection rates using small number Poisson statistics (Gehrels 1986). We have also given detection rates for different categories of objects in Table 5. In Fig. 6, we have shown the distribution of *WISE* colour $W1-W2$ vs. $W2-W3$ and radio luminosity at 1.4 GHz vs. $W2-W3$ for the combined sample. Detections are shown with filled symbols while non-detections with empty symbols.

While considering the 219 sources in the sample of Maccagni et al. (2017), which are common with that of Best & Heckman (2012b), those with $W2-W3 > 2$ have a higher detection rate than those with $W2-W3 < 2$, the values being $50.0^{+10.1}_{-8.7}$ and $13.1^{+3.6}_{-2.9}$ per cent respectively. The percentages do not change significantly if we exclude the 15

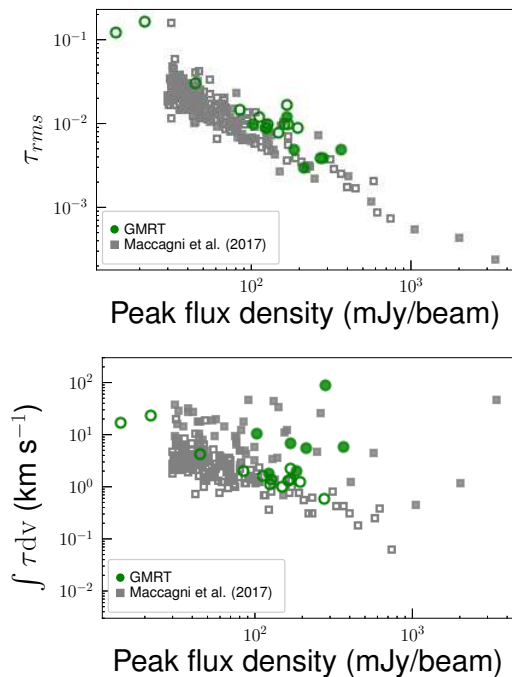


Figure 5. Top: Optical depth r.m.s vs peak flux density. 20 sources from the GMRT observations with good spectra are shown with green circles. Grey coloured squares depict 219 sources from Maccagni et al. (2017). Detections are shown with filled symbols and non-detection with empty symbols. **Bottom:** Integrated optical depth vs peak flux density. Empty symbols are $3\text{-}\sigma$ upper limits on integrated optical depth while filled symbols are estimated values from detections.

sources, which were unclassified as either LERGs or HERGs by Best & Heckman (2012b). This is consistent with our earlier work that the radio AGNs with $WISE$ colour $W2-W3 > 2$, irrespective of their accretion mode and structure, have significantly higher HI absorption detection rate than those with $W2-W3 < 2$ (Chandola & Saikia 2017).

If we consider only compact sources with $W2-W3 > 2$ classified as either LERG or HERG in Maccagni et al. (2017) sample, HI absorption detection rate is 21/36 ($58.3^{+15.7}_{-12.6}$ per cent) compared to the detection rate of 5/18 ($27.8^{+18.8}_{-12.0}$ per cent) for extended sources. They have classified sources in their sample as extended and compact using ratios of FIRST peak to integrated flux density and major to minor axis in NVSS images following the criterion used by Geréb et al. (2015). In our sample of 20 sources, which were chosen on the basis of their $WISE$ colour $W2-W3 > 2$ and have good spectra in our GMRT observations, the detection rates are $42.9^{+25.6}_{-17.0}$ per cent if we consider only the compact sources with linear projected size less than 20 kpc, and 1/6 ($16.7^{+38.3}_{-13.8}$ per cent) if we consider only the extended sources with their linear projected sizes greater than 20 kpc. The higher detection rate for those with $W2-W3 > 2$ and compact radio structure is consistent with Maccagni et al. (2017) sample, within a difference of $1\text{-}\sigma$.

The sample observed with the GMRT, shown with larger symbols in Fig. 6, all with $WISE$ colour $W2-W3 > 2$, has HI absorption detection rates of 2/8 ($25.0^{+33.0}_{-16.2}$ per cent) and 5/12 ($41.7^{+28.2}_{-18.0}$ per cent) for LERGs and HERGs respec-

tively (also see Table 5). Since detection rates have also dependence on structures, we now consider detection rates for LERGs and HERGs with only compact structures and $WISE$ colour $W2-W3 > 2$. The detection rates are 2/5 ($40.0^{+52.8}_{-25.8}$ per cent) and 4/9 ($44.4^{+35.1}_{-21.3}$ per cent) for LERGs and HERGs respectively. This shows for similar radio structure and $WISE$ colour $W2-W3 > 2$, detection rates for LERGs and HERGs are similar. However for Maccagni et al. (2017) sample, shown with smaller symbols, detection rates irrespective of their $WISE$ colours and structures are 41/189 ($21.7^{+3.9}_{-3.4}$ per cent) for LERGs and 5/15 ($33.3^{+22.5}_{-14.4}$ per cent) for HERGs. For sources with $W2-W3 > 2$ in their sample, HI absorption detection rates are 21/42 ($50.0^{+13.5}_{-10.8}$ per cent) and 5/12 ($41.7^{+28.2}_{-18.0}$ per cent) for LERGs and HERGs respectively. Further limiting their sample to the compact sources and $W2-W3 > 2$, the detection rates are 18/31 ($58.1^{+17.2}_{-13.5}$ per cent) and 3/5 ($60.0^{+58.4}_{-32.7}$ per cent) for LERGs and HERGs respectively. This again shows that for similar radio structure and $WISE$ colour, there is no difference in detection rates of LERGs and HERGs, albeit within a difference of 1σ in detection rate between our sample and the Maccagni et al. (2017) sample.

We also checked dependence of detection rates on radio luminosities. Higher radio luminosities may increase the population of hydrogen atoms with the higher spin energy level, and hence increasing the spin temperature. For the combined sample, the median radio luminosity at 1.4 GHz is $10^{24.3} \text{ W Hz}^{-1}$. We classify those below this value as low radio power sources and those above as intermediate radio power sources. According to their $WISE$ $W2-W3$ colour and radio power, we divide 219 sources in the Maccagni et al. (2017) sample into four categories, (a) low radio power and $W2-W3 < 2$, (b) low radio power and $W2-W3 > 2$, (c) intermediate radio power and $W2-W3 < 2$ and (d) intermediate radio power and $W2-W3 > 2$. The detection percentages for these categories are $13.5^{+5.1}_{-4.5}$, $55.6^{+18.4}_{-14.2}$, $12.5^{+6.2}_{-4.3}$ and $46.2^{+13.6}_{-10.8}$ showing the dependence on $W2-W3$ colour but no significant dependence on radio luminosity. Since radio structure have also significant effect, we repeat the same exercise by limiting the radio structures to compact ones. We find the detection percentages for compact radio sources in Maccagni et al. (2017) sample for above categories are $13.0^{+7.8}_{-5.2}$, $47.4^{+21.6}_{-15.5}$, $19.2^{+13.0}_{-8.3}$, $58.3^{+20.1}_{-15.4}$ respectively. Most of the sources (19/20) in our GMRT sample with good spectra are located in category of intermediate radio power with $W2-W3 > 2$ and have detection rate of $31.6^{+18.9}_{-12.5}$ per cent. If limited to compact radio structure, the detection rate increases to $38.5^{+26.0}_{-16.6}$, within $1\text{-}\sigma$ difference with Maccagni et al. (2017).

4.3 Kinematics

In order to see differences in the HI absorption profiles of two types of AGNs, we compare the parameters obtained from fitting the Busy function to the profiles such as FW20 (Full Width at 20 percent of peak), $-V_{FW20}$ (extreme blueshifted velocity relative to optical systemic velocity) and V_{centroid} (centroid shift relative to optical systemic velocity) in Fig. 7 and Fig. 8. We notice that there is no significant difference in the distribution of FW20 for HI profiles from HERGs and LERGs. However, for the HERGs, of the 10 systems only one ($10^{+23.0}_{-8.3}$ per cent) has a shift in the centroid w.r.t. optical

Table 4. Results of Busy Function fit to the HI absorption profiles

(1) Source name	(2) V_{centroid} km s^{-1}	(3) τ_{peak}	(4) FWHM km s^{-1}	(5) FW20 km s^{-1}	(6) $-V_{\text{FW20}}$ km s^{-1}	(7) $\int \tau \, dv$ km s^{-1}
J0853+0927	-258.5 ± 10.0	0.049 ± 0.003	201.2 ± 20.8	317.3 ± 22.1	-417.2 ± 14.9	10.5 ± 0.6
J0912+5320	43.7 ± 11.8	0.039 ± 0.006	51.2 ± 12.0	92.9 ± 16.6	-2.7 ± 14.4	2.4 ± 0.4
J1056+1419	16.3 ± 15.0	0.035 ± 0.004	183.7 ± 28.0	290.2 ± 34.4	-128.8 ± 22.8	7.0 ± 0.7
J1352-0156	63.8 ± 6.4	0.049 ± 0.003	49.4 ± 4.9	206.7 ± 27.7	-39.6 ± 15.3	5.2 ± 0.3
J1534+2330	-77.7 ± 0.7	0.290 ± 0.001	287.7 ± 1.1	443.3 ± 1.6	-299.3 ± 1.1	89.6 ± 0.3
J1538+5525	-36.4 ± 21.6	0.014 ± 0.002	118.1 ± 33.7	221.4 ± 41.03	-147.1 ± 29.8	2.0 ± 0.3
J2133-0712	51.2 ± 0.6	0.117 ± 0.003	53.6 ± 1.6	78.2 ± 1.7	12.1 ± 1.0	6.5 ± 0.1

Column 1: source name; column 2: velocity at centroid relative to the optical systemic velocity in km s^{-1} ; column 3: peak optical depth; column 4: full width at half maximum (FWHM) in km s^{-1} ; column 5: full width at twenty percent (FW20) in km s^{-1} ; column 6: blueshifted velocity at FW20 relative to the optical systemic velocity in km s^{-1} ; column 7: integrated optical depth in km s^{-1}

Table 5. HI absorption detection rates for different class of objects

		LERGs	HERGs	Unclassified	Total
Maccagni et al. (2017) common with Best & Heckman (2012b)					
W2–W3 <2	Compact	11/69	0/1	0/2	11/72
	Extended	9/77	0/2	0/1	9/80
	Unclassified	0/1	-	-	0/1
	Subtotal	20/147	0/3	0/3	20/153
W2–W3 >2	Compact	18/31 [†]	3/5	2/7	22/40
	Extended	3/11*	2/7	1/1	6/17
	Unclassified	-	-	4/4	4/4
	Subtotal	21/42	5/12	7/12	33/66
Total	41/189	5/15	7/15	53/219	
GMRT observed sample after excluding those with ripples					
W2–W3 >2	Compact	2/5	4/9	-	6/14
	Extended	0/3	1/3	-	1/6
Total	2/8	5/12	-	7/20	

†: 3 sources common with our GMRT observed sample, including J1435+5051 and J0906+4636.

*: 2 sources common with our GMRT observed sample.

systemic velocity more than 200 km s^{-1} . For LERGs, HI absorption profiles have a wider range (-479 km s^{-1} to $+356 \text{ km s}^{-1}$) of centroid shift values with 9/42 ($21.4^{+9.8}_{-7.0}$ per cent) having shifts either towards the blue or red end by more than 200 km s^{-1} . Most of these LERGs are intermediate radio power sources. However, for most of the HERGs with intermediate radio power except J0853+0927, this shift is less than 200 km s^{-1} . The centroid shift for most of the low power LERGs and HERGs is less than 200 km s^{-1} , except for one LERG J1638+2754. We also notice that minimum of the extreme blueshifted velocities ($-V_{\text{FW20}}$) relative to optical systemic velocities for LERGs is $\sim -619 \text{ km s}^{-1}$ compared to $\sim -417 \text{ km s}^{-1}$ for HERGs.

5 DISCUSSION

In this Section, we discuss the observed HI absorption detection rates and possible effect of AGN feedback on HI kinematics.

5.1 HI absorption detection rates

As mentioned earlier in the Section 4, we find significant dependence of HI absorption detection rates on the radio structures and *WISE* colour, which is consistent with our earlier work (Chandola & Saikia 2017). It has been discussed in previous papers in the literature that the compact radio sources allow the observer to see through higher density regions and have higher covering factor as compared to the larger radio sources, and hence increasing the detection rates (Pihlström et al. 2003; Curran et al. 2013). Also, a larger fraction of compact radio AGNs compared to extended ones are known to be residing in the gas rich host galaxies (Emonts et al. 2010).

WISE late-type galaxies with W2–W3 > 2 (Sadler et al. 2014) have relatively higher specific star formation rates than those with W2–W3 < 2 (Chandola & Saikia 2017), and hence the dust is heated due to relatively younger stellar population resulting in redder *WISE* W2–W3 colour (Donoso et al. 2012). Hence, these are relatively younger systems and are expected to have

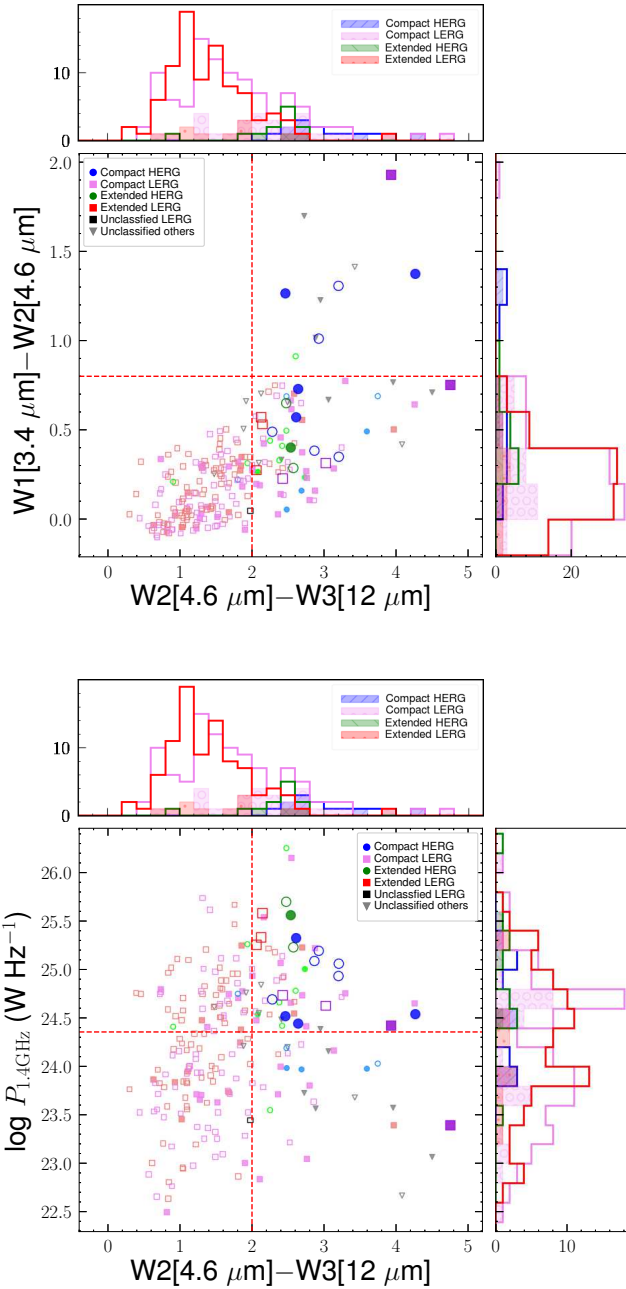


Figure 6. *WISE* W1–W2 colour (top) and luminosity at 1.4 GHz (bottom) vs *WISE* W2–W3 colour for combined sample of 233 sources. Symbols mean same as in Fig.1. Filled symbols depict HI detections while empty symbols depict HI non-detections. Histograms depict the *WISE* W2–W3 colour (top of both plots), W1–W2 colour (right of top plot) and luminosity at 1.4 GHz (right of bottom plot) distribution of LERGs and HERGs. Histograms in steps (compact HERG: blue, compact LERG: violet, extended HERG: green, extended LERG: red) show distribution of both HI detections and non-detections while shaded/hatched histograms (compact HERG: blue shade with right slash hatch, compact LERG: violet shade with circular hatch, extended HERG: green shade with left slash, extended LERG: red shade with dotted hatch) show distribution of only detections. Vertical red coloured dashed lines in both panel mark $W2-W3 = 2$. In the upper panel, horizontal red dashed line mark $W1-W2 = 0.8$, for mid-IR bright AGNs (Stern et al. 2012). In the bottom panel, horizontal red coloured line shows the median radio power (at 1.4 GHz) $\sim 10^{24.3} \text{ W Hz}^{-1}$.

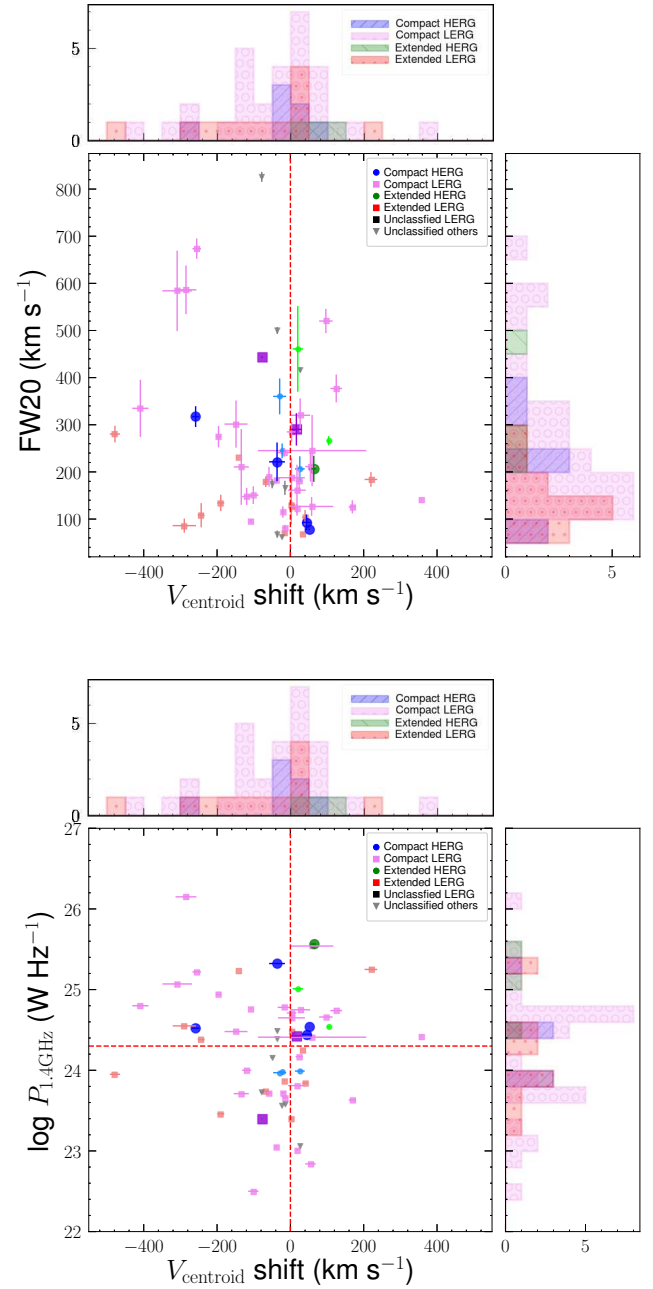


Figure 7. Full Width at twenty per cent (top) and luminosity at 1.4 GHz (bottom) vs centroid velocity relative to optical systemic velocity for 59 detections from combined sample. Symbols mean same as in Fig.1. Histograms depict the centroid shift (top of both plots), FW20 (right of top plot) and luminosity at 1.4 GHz (right of bottom plot) distribution of LERGs and HERGs from only HI detections (compact HERG: blue shade with right slash hatch, compact LERG: violet shade with circular hatch, extended HERG: green shade with left slash, extended LERG: red shade with dotted hatch). Vertical red coloured dashed lines in both panel mark $V_{\text{centroid}} = 0 \text{ km s}^{-1}$. In the bottom panel, horizontal red coloured line shows the median radio power (at 1.4 GHz) $\sim 10^{24.3} \text{ W Hz}^{-1}$.

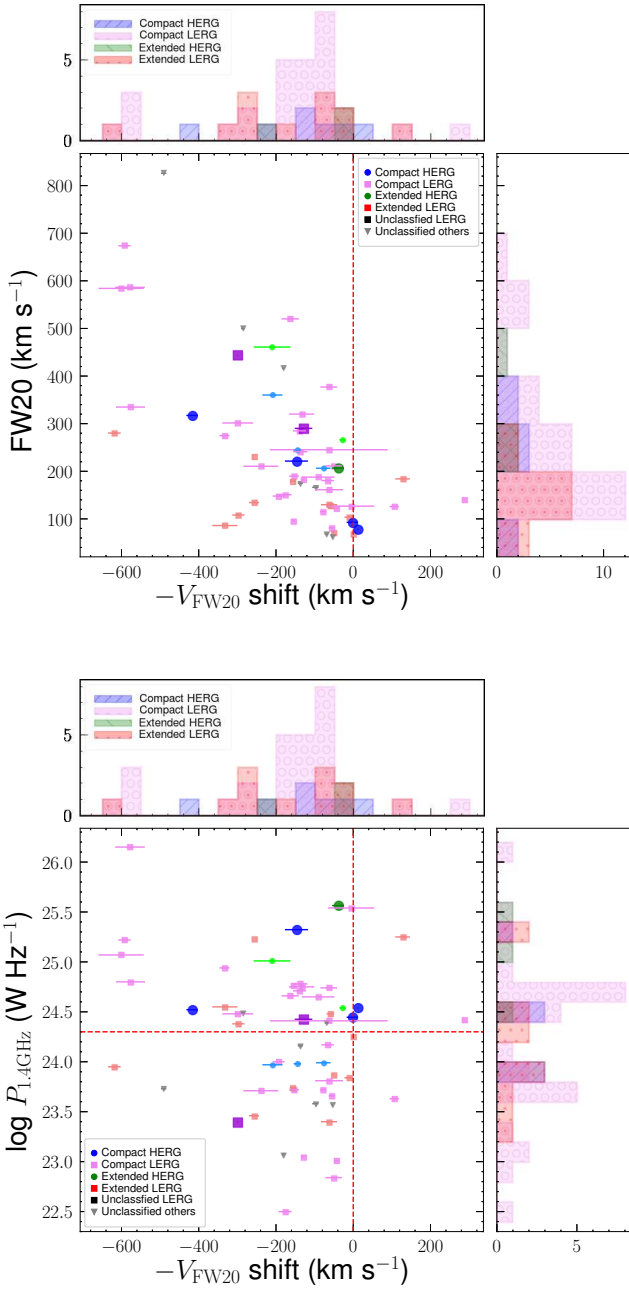


Figure 8. Full Width at twenty per cent (top) and luminosity at 1.4 GHz (bottom) vs $-V_{\text{FW20}}$ relative to optical systemic velocity for 59 detections from combined sample. Symbols mean same as in Fig.1. Histograms depict the $-V_{\text{FW20}}$ shift (top of both plots), FW20 (right of top plot) and luminosity at 1.4 GHz (right of bottom plot) distribution of LERGs and HERGs from only HI detections (compact HERG: blue shade with right slash hatch, compact LERG: violet shade with circular hatch, extended HERG: green shade with left slash, extended LERG: red shade with dotted hatch). Vertical red coloured dashed lines in both panel mark $-V_{\text{FW20}} = 0 \text{ km s}^{-1}$. In the bottom panel, horizontal red coloured line shows the median radio power (at 1.4 GHz) $\sim 10^{24.3} \text{ W Hz}^{-1}$.

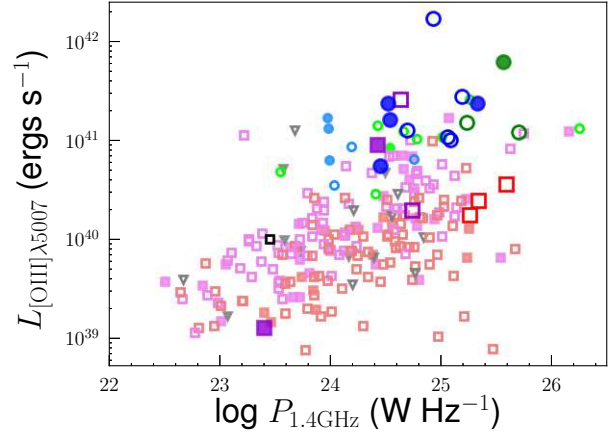


Figure 9. [OIII] $\lambda 5007$ spectral line luminosity versus radio luminosity at 1.4 GHz for combined sample of 233 sources. Symbols mean same as in Fig.1. Filled symbols depict HI detections while empty symbols depict HI non-detections.

larger amount of cold gas. Of the 204 sources classified as either LERGs or HERGs in Maccagni et al. (2017) sample common with Best & Heckman (2012b), there are 189 LERGs, of which ~ 80 per cent have $W2-W3 < 2$, while of the 15 HERGs, ~ 80 per cent have $W2-W3 > 2$. Since the host galaxies of most of the HERGs are *WISE* late type galaxies, this implies sufficient fuel in the form of cold HI gas for larger fraction of HERGs compared to LERGs. This effect of *WISE* colour along with radio structure is also reflected in the detection rates of LERGs ($22.0^{+3.9}_{-3.4}$ per cent) and HERGs ($37.0^{+15.8}_{-11.5}$ per cent) for combined GMRT and Maccagni et al. (2017) sample. However, as mentioned in the previous Section 4, we find similar HI detection rate for *WISE* late type LERGs and HERGs with compact radio structure. This implies that the detection of HI gas may not necessarily suggest the presence of high excitation mode AGN. It depends on how the cold gas is transported to the vicinity of the central engine which in turn depends on different feeding and feedback mechanisms (Martini 2004). Due to limitations of resolution of our observations and those of Maccagni et al. (2017), we are not able to put constraints on precise location of cold HI gas absorbers, and hence the mechanism for fuel transport.

5.2 Is cold gas kinematics affected by radio or optical AGN properties?

Cold gas kinematics of radio AGNs can tell us about the nature of feedback to their host galaxies. Both, radiative winds from central optical AGN, and radio jets can affect the gas kinematics in host galaxies. In this section, in order to understand the effect of both radiation and jet on gas kinematics, we compare the radio luminosity at 1.4 GHz and [OIII] $\lambda 5007$ line luminosity (using the line fluxes from MPA-JHU group) for LERGs and HERGs. While radio luminosity at 1.4 GHz can be used as tracer of jet power (Cavagnolo et al. 2010), [OIII] $\lambda 5007$ line luminosity can be used as a tracer for AGN bolometric luminosity (LaMassa et al. 2010). We find that there exists a weak but significant correlation (Kendall's $\tau=0.4$, $p=2.4 \times 10^{-16}$) between the radio luminosities and

the [OIII] $\lambda 5007$ line luminosities of LERGs (Fig. 9), which is consistent with earlier studies (Baum & Heckman 1989; Tadhunter et al. 1998), implying a common source of both luminosities. A similar correlation is noticed for HERGs but with higher [OIII] $\lambda 5007$ luminosity than LERGs for a particular value of radio luminosity, which could mean the extra energy in form of wind driven by radiation from accretion disk to cause the turbulence in host galaxy. However, in our sample of radio AGNs, while for low radio power ($P_{1.4\text{GHz}} < 10^{24.3} \text{ W Hz}^{-1}$) LERGs and HERGs, there is almost no difference in distribution of centroid shifts in the absorption profiles relative to the systemic velocity, with all but one within $\pm 200 \text{ km s}^{-1}$, a larger number of intermediate radio power ($P_{1.4\text{GHz}} \sim 10^{24.3-26.0} \text{ W Hz}^{-1}$) LERGs show centroid velocity shifts greater than 200 km s^{-1} compared to HERGs. Also the range of centroid velocity shift for LERGs is wider (-479 km s^{-1} to $+356 \text{ km s}^{-1}$) than HERGs. Although, we have doubled the number of detections compared to our previous analysis (Chandola & Saikia 2017), the overall number of sources with HI absorption detections for HERGs used for kinematic analysis is still small. Hence there are large statistical uncertainties to draw a firm conclusion about HI gas kinematics in HERGs as a population.

We further discuss possible reasons for lesser centroid velocity shifts in our sample of HERGs. We first consider the effect of radiative feedback on the HI gas kinematics. In literature, there are examples of HERGs like Mrk 231, where multiphase cold gas outflows are reported to be driven by wide angle strong radiative winds from AGN (Feruglio et al. 2015; Alatalo 2015; Morganti et al. 2016). The radiative winds in HERGs in our sample ($L_{\text{AGN}}(\text{max.}) \sim 10^{46} \text{ ergs s}^{-1}$; using the bolometric correction factor of ~ 3500 from Heckman et al. 2004 to $L_{\text{O[III]}}(\text{max.}) \sim 2 \times 10^{42} \text{ ergs s}^{-1}$), are capable of driving the galaxy scale HI outflows (King et al. 2011; Zubovas & King 2012) of kinetic luminosity $\sim 10^{42-43} \text{ ergs s}^{-1}$ as seen in Mrk 231 (Morganti et al. 2016). However, HI gas outflows like in Mrk 231 are of very shallow optical depth (Morganti et al. 2016), and hence less likely to be detected with the sensitivity of our observations. Also, radio jets are the dominant force which can drive the turbulence in host galaxies of radio AGNs in this range of luminosities (Mullaney et al. 2013; Jarvis et al. 2019; Molyneux et al. 2019). However, it depends upon how efficiently the jet couples with different phases of gas in the ISM. Simulations suggest that the coupling of jet-ISM depends on factors such as jet orientation (Cielo et al. 2018). Some other simulations suggest young radio sources with weaker inclined jets and clumpy dense interstellar medium have higher chances of interaction due to longer periods of confinement, and hence causing the turbulence (Mukherjee et al. 2018a,b). Also, differences in radio power of AGNs can give rise to the differences in distribution of velocity shifts (Chandola et al. 2011; Geréb et al. 2015; Chandola & Saikia 2017; Maccagni et al. 2017). While for the low and intermediate power LERGs, the difference in distribution of centroid shifts could be attributed to change in radio power along with jet inclination angle relative to HI disk, almost no difference in distribution for low and intermediate radio power of HERGs in our sample suggests radio power may have a lesser role to play in these HERGs. It is possible that in most of the HERGs in our sample the jets are well collimated and pierces through the inter-

stellar medium with lesser inclination compared to LERGs or radio source is too compact to interact efficiently with ISM. A better picture can be obtained by parsec scale study of these radio AGNs (Giroletti et al. 2005; Morganti et al. 2019; Jarvis et al. 2019). Also, the number of HERGs used for kinematic analysis is still small and needs to be increased from larger more sensitive surveys.

6 CONCLUSION

We summarise our findings as follows.

- We report 7 HI absorption detections towards radio AGNs from the GMRT observations, of which 6 are new.
- We find that HI absorption detection rates have significant dependence on *WISE* W2–W3 colour and radio structure. This further establishes our results from our earlier study with a much smaller sample (Chandola & Saikia 2017).
- With help of the larger sample than in our previous study, we are able to put better constraints on HI absorption detection rates for LERGs and HERGs. We find that HI absorption detection rate for HERGs ($37.0^{+15.8}_{-11.5}$ per cent) is higher than for LERGs ($22.0^{+3.9}_{-3.4}$ per cent), mainly due to a larger fraction of HERGs being hosted by gas and dust rich galaxies with younger stellar population compared to LERGs.
- For similar *WISE* W2–W3 >2 colour and compact radio structure, we don't find a significant difference in detection rate between LERGs and HERGs implying detection of HI gas doesn't necessarily mean a high accretion mode AGN. This is also consistent with our previous work.
- We don't find any significant dependence of HI absorption detections rates on radio luminosities.
- We also find that for sources of similar intermediate radio power, a larger number of LERGs, compared to HERGs, show HI absorption profiles with blue or red shift greater than 200 km s^{-1} for the centroid velocities relative to the optical systemic velocities. Also the range of velocity shift for the LERGs is larger than HERGs. This trend is consistent with that we have found in our earlier paper (Chandola & Saikia 2017). Though we have double the number of detections of HERGs compared to our earlier study, statistical uncertainties are still large in kinematic analysis. Among the possible reasons for observed distribution of centroid velocity shifts the important ones are radio source size, geometry, power, jet collimation and direction. While radio power along with jet direction may play a role for the observed difference in distribution of centroid shifts in low- and intermediate power LERGs, the difference in kinematics of both types of accretion mode AGNs could be due to differences in their interaction with the interstellar medium. This needs to be studied further from parsec scale study of these objects.

ACKNOWLEDGEMENTS

The authors thank an anonymous referee for many valuable comments and suggestions which have helped improve the paper significantly. We thank the staff of the GMRT who have made these observations possible. GMRT

is run by the National Centre for Radio Astrophysics of the Tata Institute of Fundamental Research. This work is supported by National Key R&D Program of China grant No. 2017YFA0402600. This work of YC was sponsored by the Chinese Academy of Sciences (CAS) Visiting Fellowship for Researchers from Developing Countries, Grant No. 2013FFJB0009". YC also acknowledges support from National Natural Science Foundation of China (NSFC) Grant No. 11550110181 and No. 11690024. YC also thanks Center for Astronomical Mega-Science, CAS, for FAST distinguished young researcher fellowship.

This publication makes use of data products from the *Wide-field Infrared Survey Explorer*, which is a joint project of the University of California, Los Angeles, and the Jet Propulsion Laboratory/California Institute of Technology, funded by the National Aeronautics and Space Administration. This research has made use of NASA's Astrophysics Data System. This research has made use of the NASA/IPAC Extragalactic Database (NED) which is operated by the Jet Propulsion Laboratory, California Institute of Technology, under contract with the National Aeronautics and Space Administration. This research has made use of the VizieR catalogue access tool, CDS, Strasbourg, France. The original description of the VizieR service was published in A&AS 143, 23. This work also makes use of *Sloan Digital Sky Survey* (SDSS)-III. Funding for SDSS-III has been provided by the Alfred P. Sloan Foundation, the Participating Institutions, the National Science Foundation, and the U.S. Department of Energy Office of Science. The SDSS-III web site is <http://www.sdss3.org/>. SDSS-III is managed by the Astrophysical Research Consortium for the Participating Institutions of the SDSS-III Collaboration including the University of Arizona, the Brazilian Participation Group, Brookhaven National Laboratory, Carnegie Mellon University, University of Florida, the French Participation Group, the German Participation Group, Harvard University, the Instituto de Astrofísica de Canarias, the Michigan State/Notre Dame/JINA Participation Group, Johns Hopkins University, Lawrence Berkeley National Laboratory, Max Planck Institute for Astrophysics, Max Planck Institute for Extraterrestrial Physics, New Mexico State University, New York University, Ohio State University, Pennsylvania State University, University of Portsmouth, Princeton University, the Spanish Participation Group, University of Tokyo, University of Utah, Vanderbilt University, University of Virginia, University of Washington, and Yale University.

This work has used different Python packages e.g. numpy, scipy and matplotlib. We thank numerous contributors to these packages. We have also used TOPCAT software (Taylor 2005) for this work.

REFERENCES

- Abazajian K. N., et al., 2009, *ApJS*, **182**, 543
- Abramowicz M. A., Kato S., Matsumoto R., 1989, Publications of the Astronomical Society of Japan, **41**, 1215
- Aditya J. N. H. S., Kanekar N., 2018, *MNRAS*, **473**, 59
- Aditya J. N. H. S., Kanekar N., Prochaska J. X., Day B., Lynam P., Cruz J., 2017, *MNRAS*, **465**, 5011
- Alatalo K., 2015, *ApJ*, **801**, L17
- Alatalo K., et al., 2015, *ApJ*, **798**, 31
- Allison J. R., Sadler E. M., Meekin A. M., 2014, *MNRAS*, **440**, 696
- Allison J. R., et al., 2015, *MNRAS*, **453**, 1249
- An T., Baan W. A., 2012, *ApJ*, **760**, 77
- Baldwin J. A., Phillips M. M., Terlevich R., 1981, *PASP*, **93**, 5
- Baum S. A., Heckman T., 1989, *ApJ*, **336**, 702
- Becker R. H., White R. L., Helfand D. J., 1995, *ApJ*, **450**, 559
- Berton M., et al., 2016, *A&A*, **591**, A98
- Best P. N., Heckman T. M., 2012a, VizieR Online Data Catalog, p. [J/MNRAS/421/1569](http://vizier.u-strasbg.fr/viz-bin/VizieR?source=J/MNRAS/421/1569)
- Best P. N., Heckman T. M., 2012b, *MNRAS*, **421**, 1569
- Beswick R. J., Peck A. B., Taylor G. B., Giovannini G., 2004, *MNRAS*, **352**, 49
- Brinchmann J., Charlot S., Heckman T. M., Kauffmann G., Tremonti C., White S. D. M., 2004, arXiv e-prints, pp astro-ph/0406220
- Buttiglione S., Capetti A., Celotti A., Axon D. J., Chiaberge M., Macchetto F. D., Sparks W. B., 2010, *A&A*, **509**, A6
- Cavagnolo K. W., McNamara B. R., Nulsen P. E. J., Carilli C. L., Jones C., Birzan L., 2010, *ApJ*, **720**, 1066
- Chandola Y., Saikia D. J., 2017, *MNRAS*, **465**, 997
- Chandola Y., Saikia D. J., Gupta N., 2010, *MNRAS*, **403**, 269
- Chandola Y., Sirothia S. K., Saikia D. J., 2011, *MNRAS*, **418**, 1787
- Chandola Y., Sirothia S. K., Saikia D. J., Gupta N., 2012, Bulletin of the Astronomical Society of India, **40**, 139
- Chandola Y., Gupta N., Saikia D. J., 2013, *MNRAS*, **429**, 2380
- Cicone C., et al., 2014, *A&A*, **562**, A21
- Cielo S., Bieri R., Volonteri M., Wagner A. Y., Dubois Y., 2018, *MNRAS*, **477**, 1336
- Condon J. J., Cotton W. D., Greisen E. W., Yin Q. F., Perley R. A., Taylor G. B., Broderick J. J., 1998, *AJ*, **115**, 1693
- Curran S. J., Allison J. R., Glowacki M., Whiting M. T., Sadler E. M., 2013, *MNRAS*, **431**, 3408
- D'Abrusco R., Massaro F., Paggi A., Smith H. A., Masetti N., Landoni M., Tosti G., 2014, *The Astrophysical Journal Supplement Series*, **215**, 14
- Dasyra K. M., Combes F., 2012, *A&A*, **541**, L7
- Donoso E., Best P. N., Kauffmann G., 2009, *MNRAS*, **392**, 617
- Donoso E., et al., 2012, *ApJ*, **748**, 80
- Emonts B. H. C., et al., 2010, *MNRAS*, **406**, 987
- Feruglio C., et al., 2015, *A&A*, **583**, A99
- Garwood R. W., Helou G., Dickey J. M., 1987, *ApJ*, **322**, 88
- Ge J.-Q., Hu C., Wang J.-M., Bai J.-M., Zhang S., 2012, *The Astrophysical Journal Supplement Series*, **201**, 31
- Gehrels N., 1986, *ApJ*, **303**, 336
- Geréb K., Maccagni F. M., Morganti R., Oosterloo T. A., 2015, *A&A*, **575**, A44
- Giroletti M., Giovannini G., Taylor G. B., 2005, *A&A*, **441**, 89
- Glowacki M., et al., 2019, *MNRAS*, **489**, 4926
- Gopal-Krishna Wiita P. J., 2000, *A&A*, **363**, 507
- Grasha K., Darling J., Bolatto A., Leroy A. K., Stocke J. T., 2019, *ApJS*, **245**, 3
- Gupta N., Salter C. J., Saikia D. J., Ghosh T., Jeyakumar S., 2006, *MNRAS*, **373**, 972
- Gürkan G., Hardcastle M. J., Jarvis M. J., 2014, *MNRAS*, **438**, 1149
- Gürkan G., et al., 2015, *MNRAS*, **452**, 3776
- Harrison C. M., 2017, *Nature Astronomy*, **1**, 0165
- Heckman T. M., Best P. N., 2014, *Annual Review of Astronomy and Astrophysics*, **52**, 589
- Heckman T. M., Kauffmann G., Brinchmann J., Charlot S., Tremonti C., White S. D. M., 2004, *ApJ*, **613**, 109
- Hickox R. C., Alexander D. M., 2018, *Annual Review of Astronomy and Astrophysics*, **56**, 625
- Jarvis M. E., et al., 2019, *MNRAS*, **485**, 2710
- Kauffmann G., 2018a, *MNRAS*, **473**, 5210
- Kauffmann G., 2018b, *MNRAS*, **480**, 3201
- Kauffmann G., et al., 2003, *MNRAS*, **346**, 1055
- Kennicutt Robert C. J., 1998, *ApJ*, **498**, 541

- Kewley L. J., Heisler C. A., Dopita M. A., Lumsden S., 2001, *ApJS*, **132**, 37
- Kewley L. J., Groves B., Kauffmann G., Heckman T., 2006, *MNRAS*, **372**, 961
- King A. R., Zubovas K., Power C., 2011, *MNRAS*, **415**, L6
- Kormendy J., Ho L. C., 2013, *Annual Review of Astronomy and Astrophysics*, **51**, 511
- Kunert-Bajraszewska M., Gawroński M. P., Labiano A., Siemiginowska A., 2010, *MNRAS*, **408**, 2261
- LaMassa S. M., Heckman T. M., Ptak A., Martins L., Wild V., Sonnentrucker P., 2010, *ApJ*, **720**, 786
- Lehnert M. D., Tasse C., Nesvadba N. P. H., Best P. N., van Driel W., 2011, *A&A*, **532**, L3
- Liu X., Lazio T. J. W., Shen Y., Strauss M. A., 2018, *ApJ*, **854**, 169
- Maccagni F. M., Morganti R., Oosterloo T. A., Geréb K., Maddox N., 2017, *A&A*, **604**, A43
- Mahony E. K., Morganti R., Emonts B. H. C., Oosterloo T. A., Tadhunter C., 2013, *MNRAS*, **435**, L58
- Martini P., 2004, in Storch-Bergmann T., Ho L. C., Schmitt H. R., eds, Vol. 222, *The Interplay Among Black Holes, Stars and ISM in Galactic Nuclei*. pp 235–241 ([arXiv:astro-ph/0404426](https://arxiv.org/abs/astro-ph/0404426)), doi:10.1017/S1743921304002170
- Mateos S., 2014, in Micaeliana A. M., Sanders D. B., eds, Vol. 304, *Multiwavelength AGN Surveys and Studies*. pp 209–212 ([arXiv:1401.3779](https://arxiv.org/abs/1401.3779)), doi:10.1017/S1743921314003792
- Mateos S., Alonso-Herrero A., Carrera F. J., Blain A., Severgnini P., Caccianiga A., Ruiz A., 2013, *MNRAS*, **434**, 941
- Mingo B., et al., 2016, *MNRAS*, **462**, 2631
- Mirabel I. F., 1982, *ApJ*, **260**, 75
- Molyneux S. J., Harrison C. M., Jarvis M. E., 2019, *A&A*, **631**, A132
- Morganti R., Oosterloo T., 2018, *A&ARv*, **26**, 4
- Morganti R., Oosterloo T. A., Tadhunter C. N., van Moorsel G., Emonts B., 2005, *A&A*, **439**, 521
- Morganti R., Holt J., Saripalli L., Oosterloo T. A., Tadhunter C. N., 2007, *A&A*, **476**, 735
- Morganti R., Fogasy J., Paragi Z., Oosterloo T., Orienti M., 2013, *Science*, **341**, 1082
- Morganti R., Veilleux S., Oosterloo T., Teng S. H., Rupke D., 2016, *A&A*, **593**, A30
- Morganti R., Schulz R., Nyland K., Paragi Z., Oosterloo T., Mahony E., Murthy S., 2019, arXiv e-prints, p. [arXiv:1901.01446](https://arxiv.org/abs/1901.01446)
- Mukherjee D., Wagner A. Y., Bicknell G. V., Morganti R., Oosterloo T., Nesvadba N., Sutherland R. S., 2018a, *MNRAS*, **476**, 80
- Mukherjee D., Bicknell G. V., Wagner A. e. Y., Sutherland R. S., Silk J., 2018b, *MNRAS*, **479**, 5544
- Mullaney J. R., Alexander D. M., Fine S., Goulding A. D., Harrison C. M., Hickox R. C., 2013, *MNRAS*, **433**, 622
- Mundell C. G., Ferruit P., Pedlar A., 2001, *ApJ*, **560**, 168
- Narayan R., Yi I., 1994, *ApJ*, **428**, L13
- Narayan R., Yi I., 1995, *ApJ*, **452**, 710
- Novikov I. D., Thorne K. S., 1973, in *Black Holes (Les Astres Occlus)*. pp 343–450
- Offringa A. R., 2010, AOFlogger: RFI Software, Astrophysics Source Code Library (ascl:1010.017)
- Pierce J. C. S., Tadhunter C. N., Ramos Almeida C., Bessiere P. S., Rose M., 2019, *MNRAS*, **487**, 5490
- Pihlström Y. M., Conway J. E., Vermeulen R. C., 2003, *A&A*, **404**, 871
- Plotkin R. M., Anderson S. F., Hall P. B., Margon B., Voges W., Schneider D. P., Stinson G., York D. G., 2008, *AJ*, **135**, 2453
- Sadler E. M., Ekers R. D., Mahony E. K., Mauch T., Murphy T., 2014, *MNRAS*, **438**, 796
- Salter C. J., Saikia D. J., Minchin R., Ghosh T., Chandola Y., 2010, *ApJ*, **715**, L117
- Shakura N. I., Sunyaev R. A., 1973, *A&A*, **500**, 33
- Stern D., et al., 2012, *ApJ*, **753**, 30
- Tadhunter C. N., Morganti R., Robinson A., Dickson R., Villar-Martin M., Fosbury R. A. E., 1998, *MNRAS*, **298**, 1035
- Tadhunter C., Wills K., Morganti R., Oosterloo T., Dickson R., 2001, *MNRAS*, **327**, 227
- Taylor M. B., 2005, in Shopbell P., Britton M., Ebert R., eds, *Astronomical Society of the Pacific Conference Series Vol. 347, Astronomical Data Analysis Software and Systems XIV*. p. 29
- Toba Y., et al., 2014, *ApJ*, **788**, 45
- Vermeulen R. C., et al., 2003, *A&A*, **404**, 861
- Westmeier T., Jurek R., Obreschkow D., Koribalski B. S., Staveley-Smith L., 2014, *MNRAS*, **438**, 1176
- Whittam I. H., Prescott M., McAlpine K., Jarvis M. J., Heywood I., 2018, *MNRAS*, **480**, 358
- Williams W. L., et al., 2018, *MNRAS*, **475**, 3429
- Wolfe A. M., Burbidge G. R., 1975, *ApJ*, **200**, 548
- Wright E. L., et al., 2010, *AJ*, **140**, 1868
- Yan L., et al., 2013, *AJ*, **145**, 55
- Yuan F., Narayan R., 2014, *Annual Review of Astronomy and Astrophysics*, **52**, 529
- Yuan Z. S., Han J. L., Wen Z. L., 2016, *MNRAS*, **460**, 3669
- Zubovas K., King A., 2012, *ApJ*, **745**, L34

APPENDIX A: NOTES ON INDIVIDUAL SOURCES
A1 J0028+0055

J0028+0055 is a LERG (Best & Heckman 2012b) at a redshift ~ 0.10429 , classified as radio loud narrow line Seyfert1 by Berton et al. (2016). It is a compact steep spectrum radio source. We do not find any evidence of HI absorption towards this source.

A2 J0813+0734 (4C 07.22)

J0813+0734 is a compact steep spectrum radio AGN at $z=0.11239$ classified as LERG by Best & Heckman (2012b). The SDSS optical image shows presence of disk like feature and red coloured nucleus. The HI spectrum towards this source is affected by ripples (Fig. 4). Hence, we do not consider in our main analysis. However it is possible that there is a HI absorption towards this source near optical systemic velocity which needs to be checked from observations with better sensitivity and bandpass stability.

A3 J0816+3804

This is an extended radio source with angular size $\sim 27''$ (linear projected size ~ 80 kpc). Host galaxy is a bright cluster galaxy (BCG). This source has been also searched by Maccagni et al. (2017) earlier for HI absorption, where they did not find any HI. Our result is similar to theirs with 3σ upper limit on integrated optical depth 22.8 km s^{-1} .

A4 J0832+1832

J0832+1832 is a type-2 Seyfert galaxy at a redshift of 0.15411. It is a compact flat spectrum radio source with a possible turn over at around 400 MHz which has been classified as HERG by Best & Heckman (2012b). Spectrum towards this source has been affected with ripples and hence, we do not consider the HI absorption profile towards this source for our analysis.

A5 J0853+0927

J0853+0927 is a Seyfert type 2 galaxy (Toba et al. 2014) classified as HERG by Best & Heckman (2012b) at a redshift of 0.11569. This is compact steep spectrum radio source with continuum spectra steep at higher frequency and showing turn over around 350 MHz. We detect blueshifted HI absorption line towards this source with two Gaussian components at -206 km s^{-1} and -351.1 km s^{-1} . The integrated optical depth is estimated to be $10.5 \pm 0.8 \text{ km s}^{-1}$.

A6 J0906+4636

J0906+4636 is a LERG at a redshift of 0.0847 Best & Heckman (2012b). In our earlier work we had reported HI absorption towards this source (Chandola et al. 2011). However, with the new GMRT observations we are not able to confirm our earlier result due to baseline ripple and hence do not consider in our analysis. Earlier,

Geréb et al. (2015) and Maccagni et al. (2017), had reported a non-detection towards this radio source.

A7 J0912+5320

J0912+5320 is a type-2 Seyfert galaxy at a redshift of 0.10173, with double peaked optical emission lines in SDSS spectra, classified as HERG by Best & Heckman (2012b). Radio image obtained by Liu et al. (2018) using Very Large Baseline Array (VLBA) shows subarcsecond scale structure consisting three components along north-south direction. Total angular size from VLBA image is ~ 30 mas corresponding to a linear projected size of ~ 56 parsec. We detect HI absorption line towards this source at velocity which is redshifted by $\sim 26 \text{ km s}^{-1}$ relative to the optical redshift.

A8 J1056+1419

This source has been reported as a Seyfert-1 type galaxy at redshift 0.08127 by SIMBAD astronomical database (Toba et al. 2014), but classified as LERG by Best & Heckman (2012b). In optical SDSS image, this source shows signature of merger. We detect HI absorption towards this source with two components, one deeper and broader component near systemic velocity and other shallower, narrower component redshifted by $\sim 158.2 \text{ km s}^{-1}$. The narrower redshifted component could be due to infalling gas cloud.

A9 J1058+5628

J1058+5628 is classified as BLLac object by Plotkin et al. (2008) and LERG by Best & Heckman (2012b). The redshift of this source in SDSS is 0.14324. This is another source for which the HI spectrum has been affected by ripples.

A10 J1107+1825

J1107+1825 is a Seyfert type-1 galaxy at redshift 0.17856. It has been classified as HERG by Best & Heckman (2012b). It has also a nearby galaxy with unknown redshift in SDSS optical image. HI spectrum towards this source is also affected by ripples.

A11 J1110+2131

J1110+2131 is also a Seyfert type-1 galaxy (Toba et al. 2014) and a compact steep spectrum radio source at a redshift of 0.13461 and classified as HERG by Best & Heckman (2012b). We do not detect HI absorption towards this source as well.

A12 J1156+2632

J1156+2632 is Seyfert type-2 galaxy (Toba et al. 2014) at a redshift of 0.15625. It is classified as HERG by Best & Heckman (2012b). It is a compact flat spectrum radio source. We do not detect HI absorption towards this radio source.

A13 J1217-0337

PKS 1215-033 is a HERG at redshift of 0.18229 (Best & Heckman 2012b). This source has resolved structure with GMRT beam of angular size $\sim 9.68''$, which corresponds to 29.68 kpc in projected linear size. This source has not been detected with HI absorption.

A14 J1328+1738

J1328+1738 is a Seyfert type-1 galaxy (Toba et al. 2014) classified as HERG by Best & Heckman (2012b). It is located at a redshift of 0.18035 and could be classified as compact flat spectrum radio source based on ViZieR radio flux values. We report a HI non-detection towards this source. However, it is possible that there is marginal HI absorption towards this source near optical systemic velocity which needs to be checked from observations with better sensitivity.

A15 J1341+5344

J1341+5344 is a Seyfert type-2 galaxy (Toba et al. 2014) at a redshift of 0.14094, classified as HERG by Best & Heckman (2012b). This is an extended radio source of angular size $\sim 1.52''$ which corresponds to a projected linear size of ~ 226 kpc. We do not detect HI absorption towards the brightest pixel in the central region of this source.

A16 J1350+0940

J1350+0940 is bright cluster galaxy (BCG) (Yuan et al. 2016) at a redshift of 0.13255, classified as Seyfert type-1 galaxy by (Toba et al. 2014). It has been also classified as LERG by Best & Heckman (2012b). Using radio fluxes obtained from ViZieR, it could be classified as either GPS or CFS radio source. HI spectrum towards this source is affected by a broad ripple across the band, and hence not included in our analysis. It is possible that there is a very shallow, wide and blueshifted HI absorption profile towards this source. This possibility needs to be checked from more sensitive observation.

A17 J1352-0156

PKS J1352-0156 is a radio galaxy at a redshift of 0.16694, classified as HERG by Best & Heckman (2012b). It is an intermediate radio power AGN ($L_{1.4\text{GHz}} \sim 10^{26}$ W/Hz). This source has resolved structure of $\sim 9''$ with GMRT beam of $\sim 2''$. This corresponds to a projected linear size of ~ 26 kpc. The HI absorption profile towards this source has two components, one narrow and deep, other wide and shallow, both redshifted w.r.t. the optical emission lines. The wide profile has full width half maximum of ~ 300 km s $^{-1}$ and is redshifted by ~ 44 km s $^{-1}$. Narrower profile is redshifted by ~ 146 km s $^{-1}$ and has FWHM ~ 39 km s $^{-1}$. The peak optical depths for narrower and broader profiles are 0.041 and 0.013, respectively. Integrated optical depth estimate for this source is 5.8 ± 0.4 km s $^{-1}$ which corresponds to a column density of $10.6 \pm 0.7 \times 10^{20}$ cm $^{-2}$, if we assume $T_s = 100$ K and $f_c = 1$.

A18 J1400+5216

J1400+5216 is a Low Ionization Nuclear Emission-line Region (LINER) galaxy at a redshift of 0.11789, classified as LERG by Best & Heckman (2012b). This source was also observed by Maccagni et al. (2017) where they report a non-detection of HI absorption. We also do not detect HI absorption with an upper limit of 2.3 km s $^{-1}$ on integral optical depth corresponding to 4.1×10^{20} cm $^{-2}$ for $T_s = 100$ K and $f_c = 1$.

A19 J1410+1438

J1410+1438 is a BLLac object (D'Abrusco et al. 2014) at a redshift of 0.14419 classified as LERG by Best & Heckman (2012b). The radio continuum image suggests this is an extended radio source with angular size $\sim 22''$ or linear projected size ~ 55 kpc. We do not detect HI absorption towards this source as well.

A20 J1435+5051

J1435+5051 is a radio galaxy at a redshift of 0.09969. It is classified as LERG by Best & Heckman (2012b). This source was also observed by Maccagni et al. (2017) where they report a detection of HI absorption with a shift on centroid of -66.7 km s $^{-1}$ relative to optical systemic velocity. However, from our observation we are not able to confirm it, possibly due to higher noise in our spectra.

A21 J1447+4047

J1447+4047 is a radio galaxy at a redshift of 0.19515 which has been classified as LERG by Best & Heckman (2012b). It is an extended radio source with overall angular size of $\sim 14.6''$ corresponding to projected linear size of 47.3 kpc. This source has been also searched for HI absorption by Maccagni et al. (2017) with no detection. We also do not detect HI absorption towards this source.

A22 J1449+4221

J1449+4047 is a Seyfert type-2, compact flat spectrum radio source at a redshift of 0.17862 classified as LERG by Best & Heckman (2012b). We do not detect HI absorption towards this radio source.

A23 J1534+2330

J1534+2330 or Arp 220, is a dust rich Ultra-luminous infrared galaxy (ULIRG) system of spiral galaxies which has undergone recent merger at redshift of 0.0184. This source has been classified as LERG by Best & Heckman (2012b). We detected HI absorption profile with multiple components towards this source for which the HI column density estimate is $163.0 \pm 0.9 \times 10^{20}$ cm $^{-2}$ for $T_s = 100$ K and $f_c = 1$. HI absorption towards this source has been detected in earlier works as well (Mirabel 1982; Garwood et al. 1987; Mundell et al. 2001; Allison et al. 2014). Mundell et al. (2001) from their parsec scale study reported absorption against two continuum nuclei due to two counter rotating HI disks and bridge of gas connecting them.

A24 J1538+5525

J1538+5525 is type-1 Seyfert galaxy at a redshift of 0.19117, with double peaked narrow optical emission lines detected in SDSS spectra (Ge et al. 2012). It has been classified as HERG by Best & Heckman (2012b). It is also a compact steep spectrum radio source. We detected HI absorption towards this source where the profile can be fitted with two Gaussian components, both blueshifted relative to optical systemic velocity. The narrower and deeper component is blueshifted by $\sim 105 \text{ km s}^{-1}$ while broad, shallow component is blueshifted by $\sim 49 \text{ km s}^{-1}$.

A25 J1543+0235

J1543+0235, is a Seyfert type-2 galaxy at a redshift of 0.18793, classified as HERG by Best & Heckman (2012b). This is an extended radio source in GMRT continuum image with resolved structure of $\sim 11.9''$ which corresponds to $\sim 37 \text{ kpc}$ in linear projected size. HI spectrum towards this source is also affected by ripples.

A26 J1559+5330

J1559+5330 is also a Seyfert type-2 galaxy (Toba et al. 2014) at a redshift of 0.17919 which has been classified as HERG by Best & Heckman (2012b). We do not detect HI absorption towards this source.

A27 J2133-0712

J2133-0712 is radio galaxy at a redshift of 0.08654, classified as HERG by Best & Heckman (2012b) with disc shaped morphology in SDSS optical image. We detect HI absorption towards this source with single Gaussian component redshifted by $\sim 51 \text{ km s}^{-1}$ relative to optical systemic velocity.

This paper has been typeset from a $\text{\TeX}/\text{\LaTeX}$ file prepared by the author.